2

DOT/FAA/NR-93/5

Program Director
For Surveillance
Washington, D.C. 20591

Investigation of Outflow Strength Variability in Florida Downburst Producing Storms

February 1993

Final Report

This document is available to the public through the
National Technical Information Service,
Springfield, Virginia 22161.

U.S. Department
of Transportation
**Federal Aviation
Administration**

119P0

DISCLAIMER NOTICE

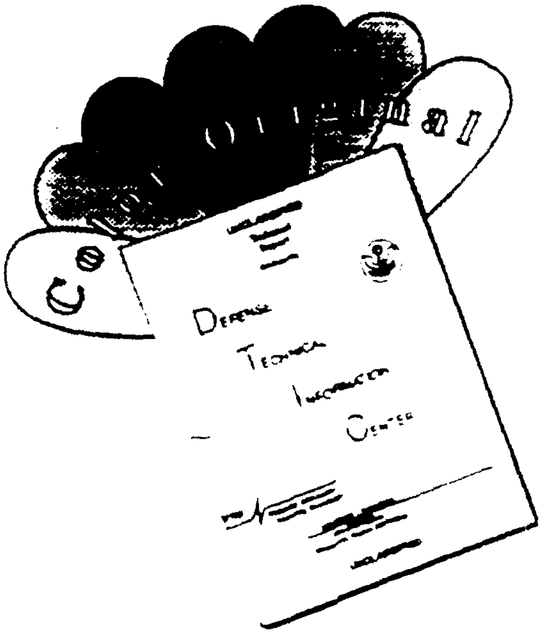

Technical Report Documentation Page

1. Report No. DOT/FAA/NR-93/5	2. Government Accession No.	3. Recipient's Catalog No.
4. Title and Subtitle Investigation of Outflow Strength Variability in Florida Downburst Producing Storms		5. Report Date February 1993 6. Performing Organization Code
7. Author(s) J. T. Johnson, Michael Eilts, Kevin Droegemeier		8. Performing Organization Report No.
9. Performing Organization Name and Address Forecast Applications Research Group National Severe Storms Laboratory Norman, Oklahoma		10. Work Unit No. (TRAIS) 11. Contract or Grant No.
12. Sponsoring Agency Name and Address U.S. Department of Transportation Federal Aviation Administration Program Director for Surveillance Washington, D C. 20591		13. Type of Report and Period Covered Final Report 14. Sponsoring Agency Code ANR-150
15. Supplementary Notes		

16. Abstract

With the Federal Aviation Administration introducing Doppler weather radar to high-traffic airports in the form of the Terminal Doppler Weather Radar (TDWR), improved identification of dangerous windshears from downbursts and other weather phenomena will be possible. Using detection and prediction algorithms, the TDWR system will give controllers and pilots more information about the weather situation in the terminal area than is available heretofore.

During the summer of 1990, a prototype TDWR system was tested and evaluated in Orlando, Florida with more than 500 downbursts detected. Many storms possessing apparently "similar" characteristics were found to produce a wide variety of outflow speeds on days with nearly the same environmental structure. In this study, we use single-Doppler radar observations, surface mesonet data and a 3-D numerical cloud model in an attempt to determine causes for the observed variability. In particular, we examine 8 downbursts from August 18, 21 and 22 as well as 5 simulated downbursts.

Our results show that the observed variability is explained neither by Doppler radar signatures known to precede downbursts (e.g., convergence and rotation aloft) nor by minor but detectable variations in the environment among the three days examined. Suspecting somewhat more subtle mechanisms, we examined detailed microphysical processes within numerically simulated storms. Though we identified three important regimes associated with downburst production (above melting level, between melting level

17. Key Words Terminal Doppler Doppler Radar Weather Windshear Downbursts	18. Distribution Statement This document is available to the public through the National Technical Information Service, Springfield, Virginia 22161.

19. Security Classif. (of this report) Unclassified	20. Security Classif. (of this page) Unclassified	21. No. of Pages 111	22. Price

Form DOT F 1700.7 (8-72)

Reproduction of completed page authorized and cloud base, and below cloud base), no clear ties were found between microphysics variations and the intensity of the outflows.

By eliminating the above mechanisms, we reason that the observed variability, which at times is quite significant, could perhaps be explained by very shallow surface-based stable layers whose principle effect would be to diminish outflow intensity through dispersion of energy by gravity waves. Numerical simulations of clouds growing in such environments verified this hypothesis, and showed that although updraft and downdraft intensity are virtually unaffected relative to a non-stable-layer simulation, the resulting outflow speed can be reduced by as much as 40%.

ACKNOWLEDGEMENTS

Thanks go to Drs. Conrad Ziegler of NSSL and Jerry Straka of the University of Oklahoma for editing of the manuscript. Thanks also go to Kelly Lynn for her help in putting figures together. Some figures were wonderfully drafted by Joan Kimpel. Many people within the Forecast Applications Research group of NSSL contributed their talents to make this study possible. Group 43 of MIT Lincoln Laboratory (MIT/LL) and the University of North Dakota radar group collected the radar data used in this study. MIT/LL also provided the initial post-processing and software tools for analysis. Data used in this report were provided by MIT/LL under sponsorship from the Federal Aviation Administration.

TABLE OF CONTENTS

Page

CHAPTER

LIST OF ILLUSTRATIONS

LIST OF TABLES

CHAPTER I

INTRODUCTION

The term "downburst" was coined by Fujita and Byers (1977) to describe unusually intense, small-scale convective downdrafts having vertical velocities greater than 12 ft/s (~4 m/s) at an altitude of 300 ft (~100 m) AGL. As the descending column of negatively-buoyant air nears the ground, vertical momentum is converted to horizontal momentum and accelerated radially by pressure gradient forces, resulting in horizontally-divergent, shallow outflow patterns that can exhibit wind speeds in excess of 40 m/s. Fujita and Byers further subdivided downbursts into *macrobursts* (downbursts having diameters greater than 4 km and lasting from 5 to 30 min) and *microbursts* (downbursts having diameters less than 4 km and lasting only 2 to 5 min). In this study we make no distinction between the mechanisms of a typical thunderstorm downdraft and those of a downburst. However, we define downbursts as surface outflow events with a divergent Doppler radar differential radial velocity (ΔV) of 10 ms^{-1} or greater.

Downbursts are particularly noteworthy because of the danger they pose to both private and commercial aviation. During the past 20 years, at least 7 major aircraft accidents involving over 400 deaths have been attributed directly to downbursts, with numerous non-fatal incidents occurring yearly (e.g., Wolfson, 1990). The Federal Aviation Administration (FAA) has recognized the potential hazard that downbursts present and will have spent over $27 billion by the year 2000 in modernizing and automating the U.S. air-traffic control system (Shantz, 1991). A portion of this spending (~ $2 billion) is budgeted for weather detection sensors such as the Terminal Doppler Weather Radars (TDWR) and Low-Level Wind Shear Alert Systems (LLWAS) at major airports around the United States. Both TDWR and LLWAS will provide much improved detection of downbursts within the terminal area. The effective use of these and other new observing tools is greatly dependent upon an understanding of low-altitude windshear phenomena, for example downbursts and gust fronts, both of which pose a significant low-altitude threat to aviation.

Computer algorithms have been developed for both downburst and gust front detection using Doppler radar data (e.g., Merritt, 1990; Eilts, et al. 1991). Detection is important in the terminal area, but prediction is a much more difficult task. Campbell (1991) describes the Microburst Prediction (MBP) product and its proposed use with TDWR. The current MBP product uses TDWR data to search for microburst precursors (i.e., signatures that satisfy certain space and time continuity constraints) of mid-altitude convergence, high reflectivity core aloft, mid-level rotation or upper-level divergence. *The present TDWR MBP product attempts to predict downburst timing and location, and* *not strength.*[1]

During June, July, and August of 1990, the FAA held an Operational Test and Evaluation (OT&E) of a prototype TDWR system in Orlando, Florida as part of the radar's on-going development. This project utilized two 5-cm Doppler radars, operated by Lincoln Laboratory (FL-2C) and the University of North Dakota (UND). Upper-air soundings were taken by the National Severe Storms Laboratory's (NSSL) mobile sounding system, and a surface mesonet was also in place. The layout for the 1990 TDWR OT&E is shown in Figure 1.1.

Inspection of Doppler radar data from the 1990 TDWR OT&E reveals that storms of similar reflectivity structure, occurring in similar environments, often produced downbursts of very different strength, with low-altitude Doppler measured velocity difference across the downburst (ΔV) varying anywhere from 10 to 40 m/s. *As part of the important task of understanding downbursts, this study will utilize Doppler radar data, soundings, mesonet data and a 3-D numerical cloud model to investigate eight downburst-producing storms in an effort to gain insight into the cause of this variability. It is proposed that information from this study may benefit further development of a MBP product as well as our general understanding of convective outflows.*

---

[1] MIT Lincoln Laboratory is currently developing a MBP algorithm that incorporates available environmental temperature data to allow a strength prediction to be made. Preliminary results are encouraging (Wolfson, personal communication).

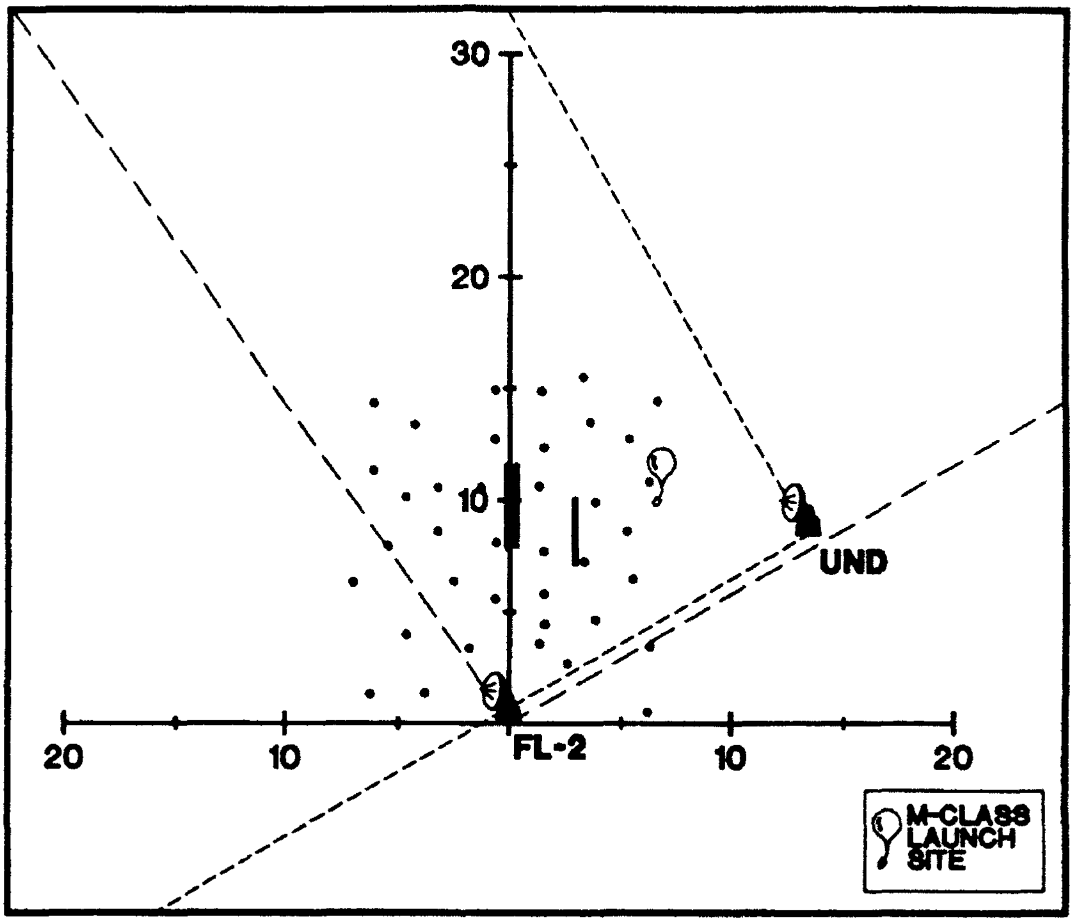

Figure 1.1 Layout of sensors for the 1990 Terminal Doppler Weather Radar (TDWR) Operational Test and Evaluation (OT&E) held in Orlando, Florida during June - September. Dashed line extending from the radars represent the nominal scanning sectors for each of the radars. The balloon symbol is the location of the sounding launches and the dots represent the surface mesonet sites. See text for details concerning the radars FL-2C and UND.

In Chapter 2, we review previous studies into the phenomenon of downbursts and discuss how the present work contributes to our understanding. Chapters 3 and 4 discuss details of the method and results of the observational and modeling portions, respectively. Chapter 5 summarizes, provides conclusions and makes conjectures concerning the importance of the findings.

CHAPTER II

BACKGROUND AND RATIONALE

2.1 *Background*

Previous studies have provided insight into physical mechanisms that are responsible for downbursts and contributed to improved observing and nowcasting techniques for downbursts. Processes of precipitation drag (Krumm, 1954; etc.), evaporational cooling and cooling by melting (Knupp, 1985; Srivastava, 1985; Chen, 1986; Krueger, et al., 1986; Proctor, 1988; etc.) as well as entrainment (Braham, 1958; Knupp, 1985; etc.) have been associated with downburst formation and maintenance. Many of these studies utilized numerical models which have proven successful in confirming the theoretical physical processes and have quantified the relative importance and sensitivity of such processes for a variety of environmental settings. The discovery of Doppler radar velocity and reflectivity precursors to downbursts and their inclusion in algorithms have increased the short-term prediction skill for downburst events (Campbell, 1991). However, there remain some unanswered questions concerning differences that are observed in storms having similar reflectivity structure and maximum.

2.2 *Rationale*

A higher reflectivity storm is typically considered capable of producing a stronger outflow than one having weaker reflectivity in a similar environment since more liquid water can lead to more precipitation loading, evaporation, etc. A relationship between the reflectivity and the liquid water content is given by Greene and Clark (1972) as

$$R_c = 3.44x10^{-3}Z^{(4/7)} \tag{2.8}$$

where R_c is the liquid water content in units of g m^{-3} and Z is the radar reflectivity in units of mm^6 m^{-3}. Equation (2.8) is a Z-R_c relationship using a Marshall-Palmer exponential drop-size distribution. Radar meteorologists typically use a logarithmic scale for reflectivity (units of dBZ), so if the R_c-Z relationship given by (2.8) is used, a reflectivity of 50 dBZ is produced by a liquid water content of 2.5 g m^{-3}. An increase to only 55 dBZ requires nearly twice as much liquid water (4.8 g m^{-3}). Thus, when initially examing two storms the higher reflectivity storm would be considered capable of producing a stronger outflow than a storm having weaker reflectivity in a similar environment.

In this study, we use single-Doppler radar observations, upper air soundings and surface mesonet data in an attempt to determine causes for the observed variability in the downburst-producing storms observed in the 1990 TDWR OT&E. Tables 2.1 - 2.3 provide a listing of the downbursts that were observed by radar meteorologists viewing real-time displays of the FL-2C Doppler radar on August 18, 21 and 22. The apparent lack of a relationship between the maximum reflectivity and the strength of outflow

Table 2.1 Downbursts observed with the FL-2C radar on August 18, 1990. Starred downbursts (*) are cases investigated further in this study. Reflectivity is peak reflectivity at the lowest elevation angle.

Time (UTC)	Azimuth/Range	ΔV (ms^{-1})	Reflectivity
1920	004/31	11	45
*1924	012/30	12	50
1935	078/26	14	50
*1946	030/19	14	50
1949	084/19	14	50
*1954	027/21	16	50
*1955	048/20	10	50
1956	359/27	23	35
2011	027/12	17	50
2011	014/27	16	50
2017	010/13	30	50
2019	040/10	18	50
2036	106/15	19	50
2036	121/20	13	55
2045	269/21	20	50
2045	131/18	12	50

Table 2.2 As in Table 2.1, except for August 21, 1990.

Time (UTC)	Azimuth/Range	$\Delta V(ms^{-1})$	Reflectivity
2157	310/23	14	55
*2201	347/31	10	52
2209	321/32	12	50
2210	352/29	10	50
*2218	342/17	27	55
2224	351/13	12	50
2231	009/22	10	50
2243	012/28	14	50
2248	343/9	10	55
2254	355/12	10	55
2256	023/22	12	50
2346	046/10	20	55
2347	044/11	14	55

Table 2.3 As in Table 2.1, except for August 22, 1990.

Time (UTC)	Azimuth/Range	ΔV (ms^{-1})	Reflectivity
2042	345/10	40	50
*2042	262/18	25⁺	50
*2100	005/20	30	50
2101	278/15	14	50
2106	348/2	22	50
2124	244/11	30	55
2137	042/26	24	50
2155	061/35	20	55
2206	222/20	16	45
2246	146/23	20	50

⁺ - UND data used; downburst occurred outside FL-2C scanning sector.

demonstrates the variability that was observed. Some high reflectivity storms produced weak outflows, while others some produced strong outflows, there are similar results for low reflectivity storms. Overall, downbursts on August 22 were stronger than the other two days, with August 18 slightly stronger than August 21.

2.3 *Hypotheses*

Based on past studies, several hypotheses for the observed variability in outflow strength of apparently similar storms can be proposed. Differences in radar-detected precursors (e.g. mid-altitude convergence and rotation) in downburst-producing storms could be correlated with the observed variability in outflow strength. Also, differences in the environment, as given by the upper air soundings, could possibly explain the variability. Differences in the individual storms (e.g. absolute water/ice content and relative amount of liquid vs. ice or the shape of the storms) could cause differences in the physical mechanisms that force the downburst. Additionally, the presence of ground-based stable layers could cause a damping of the outflow speed from a storm.

Previous studies (e.g., Roberts and Wilson, 1986; Eilts, 1987) have investigated downburst precursors to try to correlate the occurrence of the precursors and the subsequent downburst. Eilts (1987) examined the strength of the convergence precursor and compared it to the strength of the downburst. He found that the convergence aloft was roughly half as strong as the resultant outflow for the Oklahoma downbursts investigated. We will examine the precursors for the 8 Florida downbursts in a similar manner to discern whether differences in the precursors can possibly explain the observed differences in outflow strength.

Differences in the environment that the storms develop could also explain the variability. In a day-to-day comparison of the outflow observations, an examination of the soundings of the days could give insight into why the variability exists. One would expect that differences in the soundings for a Florida summertime environment would be only slight since sub-tropical regions, such as Florida, do not experience significant environmental changes very often. We will examine the soundings for the three individual days in this study to determine whether the differences in outflow strength can be explained by differences in the sounding

Could differences in individual storms explain the observed variability? These differences in the storms can be quantified by examining the microphysical forcing that takes place in the storm (e.g. evaporational cooling, cooling by melting, etc.). We will perform numerical simulations of storms on the three days to determine if the differences in the observed outflows can possibly be explained by differences in the microphysical forcing.

A near-surface stable layer existing underneath a storm that produces a downburst could cause the downburst to be attenuated and thus not allow the outflow to reach its maximum potential. Proctor (1989), Wolfson (1990) and Droegemeier (1991) have documented this effect and it will be investigated in this study by performing additional numerical simulations in which downdrafts are allowed to fall into low-altitude stable layers. These simulations will raise some questions concerning strength variability that need to be examined for TDWR and NEXRAD applications research and development.

CHAPTER III

OBSERVATIONAL STUDY

3.1 *Objective*

In this portion of the study we investigate the Doppler radar reflectivity and velocity fields of 8 downburst-producing storms in an attempt to explain the observed variability and to examine the possibility of using precursors to predict the variability.

3.2 *Data*

3.2.1 *Radar data*

The Doppler radar data used in this study were provided by the Massachusetts Institute of Technology's (MIT) Lincoln Laboratory under sponsorship from the FAA. Data from both FL-2C and UND were analyzed (see Figure 1.1 for radar locations). These data were collected with high resolution in both time and space with low-altitude scans taken every 1 minute using a gate spacing of 150 m and an azimuthal separation of 1 deg. Full volume scans were collected every 2.5 minutes. Further information about the radar scanning strategies is listed in Table 3.1 and specific characteristics of the two

Table 3.1 1990 TDWR OT&E radar scanning strategies.

Radar	Elevation angles in order of occurrence (deg)	Nominal scanning sector (deg)
FL-2C	0.5 3.3 6.7 10.0 13.2 17.2 22.3 0.4 1.0 28.7 36.2 0.4 44.3 52.4 3.3 6.7 10.0 0.4 13.2 17.2 22.3 28.7 36.2 0.4 44.3 52.4 60.0	330 - 060
UND	0.5 1.0 3.3 0.4 6.7 10.0 13.2 17.2 22.3 28.7 0.3 36.2 44.3 52.4 60.0	225 - 340

Table 3.2 Radar characteristics of 1990 TDWR OT&E radars.

Radar	Wavelength (cm)	Gate Spacing (m)	Beam Width (deg)	*Nyquist Velocity (ms^{-1})
FL-2C	5	150	0.5	16 - 22.5
UND	5	150	1.0	15

*For cases analyzed

pencil beam Doppler radars are listed in Table 3.2.

3.2.2 *Sounding data*

Upper air soundings were taken from a location ~5 km NE of UND (see Figure 1.1). Scheduled sounding times were 1100 UTC, 1400 UTC and 1700 UTC with additional soundings being released if convection was probable near Orlando. These soundings contain temperature and relative humidity as well as wind speed and direction every 10 m in height.

3.2.3 *Mesonet data*

Surface data were collected at 40 mesonet and LLWAS sites (Stoll, 1991) in an area approximately 56 km^2 surrounding the Orlando International Airport (see Figure 1.1). Temperature, relative humidity, station pressure, wind speed and direction and precipitation amount were measured and recorded at each site at 1 minute intervals.

3.2.4 *Limitations of observational data*

Because only single Doppler radar data are used in this study, only the radial component of the horizontal velocity field is available. Asymmetry does exist in the surface outflows and the strongest shear across the outflow is not always sampled by the single radar. A lower bound on the asymmetry will be estimated by comparing the outflow strengths from the two radars (FL-2C and UND).

None of the 8 downbursts examined occurred within the mesonet; thus, a true picture of the surface conditions before or during the downburst events is difficult to attain. However, since all 8 of the analyzed downbursts were within 20 km of the mesonet, the mesonet data will be used to qualitatively ascertain the approximate surface conditions.

The amount and type of data used in this study are similar to those that will be available in an operational aviation weather setting with a TDWR, except that a surface mesonet will not generally be available at each airport. The TDWR system will integrate LLWAS information to produce hazard warnings, but these stations do not make temperature or relative humidity measurements and are fewer in number than the mesonet used in the TDWR OT&E.

The examination of only 8 downburst cases is also a limitation since the "correlations" between storm characteristics and outflow strength will not be statistically significant. Nevertheless, we feel that these cases are representative of downburst-producing storms for the days under investigation.

3.3 *Method*

3.3.1 *Selection of downburst cases*

Downburst events were chosen for analysis if they were relatively isolated from other storms, within 35 km of the radar and if a sounding was available within 4 hours of the downburst event. The definition of "isolated" is, of course, subjective, but is based on whether a storm's mid- and upper-altitude wind field appeared to interact significantly with other storms. We chose to examine isolated storms so as to avoid possible complications in understanding the observed variability.

The other principle requirement is that a storm's entire life cycle (first echo to maximum outflow) had to take place within 35 km of the radar. This condition was chosen because of the shallowness of the surface outflows associated with downbursts (Wilson et al, 1984; Hjelmfelt, 1988). If a storm is too distant from the radar, the strongest shears may not be sampled by the radar due to both earth and radar beam curvature effects causing the beam to be higher than the strongest outflow. The distance of 35 km was chosen as the range limit because, at an elevation angle of 0.4° (lowest elevation angle in the FL-2C scanning strategy), the center of the radar beam is ~250 m AGL and the strongest divergence associated with High Plains downbursts has been shown to occur below 300 m AGL (Wilson et al., 1984) and the median depth of outflows in Southeast US storms was 450 m AGL in a study by Biron and Isaminger (1991).

3.3.2 *Processing of sounding data*

Soundings from 1700 UTC were analyzed to obtain the following information:

1. Lifted Index (LI)
2. Convective Available Potential Energy (CAPE)
3. Convective Condensation Level (CCL)

4. Lifted Condensation Level (LCL)
5. Precipitable water
6. Height of melting level

A complete discussion of the above sounding parameters and characteristics is given in Appendix A of Johnson (1992).

3.3.3 *Processing of radar data*

Each individual radar tilt was analyzed from the first echo of the thunderstorm that produced a downburst (as the radar data allowed) and the following were noted:

1. type of velocity feature (convergence, divergence or rotation) and time of occurrence,
2. differential radial velocity (ΔV) of feature,
3. horizontal extent of velocity feature (peak-to-peak),
4. range of velocity feature,
5. height of velocity feature and
6. reflectivity in the vicinity of velocity feature.

A minimum threshold of 4 m s^{-1} was chosen for the differential radial velocity of convergence and rotation aloft taken as a peak to peak difference. This threshold, while considerably lower than that used in previous studies by Isaminger (1990) and others, was chosen so as to not eliminate features with ΔV's less than 10 m s^{-1}. A choice of threshold under 4 m s^{-1} was considered too small and approached the noise level of the velocity data. The reflectivity in the vicinity of the velocity feature was noted for the purposes of indicating reflectivity features such as notches and descending cores.

The liquid water content of a cloud can be used to determine the amount of condensation and dynamic development that has taken place. Changes in the liquid water content are also associated with thermodynamic energy changes (Greene and Clark, 1972). Vertically integrated liquid water (VIL), a measure of the liquid water in a vertical column within a storm, was calculated using the reflectivity data. VIL is given by

$$VIL = \sum_{i=1}^{n} 3.44x10^{6} \left(\frac{[Z_i + Z_{i+1}]}{2}\right)^{4/7} \Delta h \qquad [kg\ m^{-2}] \tag{3.1}$$

where Z_i and Z_{i+1} are reflectivity factors at two successive levels and Δh is the distance (m) between the levels (Stewart, 1991). Thus, VIL increases with both the magnitude and depth of the reflectivity. For National Weather Service purposes, VIL is calculated within 3 X 5 km horizontal 'bins' (Stewart, 1991). However, in this study we calculate VIL by taking a horizontal average of reflectivity over an area 3 X 3 km centered on the maximum reflectivity at each level, and then vertically integrate through the depth of the storm. This method, hereafter known as slantwise VIL, was chosen to account for any tilt that may be present within the core of the storm. Slantwise VIL is, in no way, meant to imply that a downdraft would fall along a slanted vertical path. It is simply a measure of the liquid water content of the reflectivity core that may not be entirely captured by a normal VIL calculation. Slantwise VIL calculations were performed at least 3 volume scans (7.5 minutes) prior to initial outflow and every 5 minutes thereafter. These calculations were performed in order to determine if a meaningful relationship existed between the slantwise VIL and the resultant outflow strength.

As an analysis tool, we calculated the three-dimensional mass of each storm for at least 3 volume scans prior to initial outflow through the time of maximum outflow. Assuming a Marshall-Palmer distribution, the storm mass was calculated using the same Z-R relationship (Greene and Clark, 1972) used in the slantwise VIL calculations. One would expect that the mass of a storm would increase as a storm is growing and then decrease as the reflectivity core descends and outflow is produced. However, there may be some value in examining the mass in relation to the strength of an outflow.

An additional feature of the downburst-producing storms investigated is the aspect ratio (depth/width) of the reflectivity core. Other studies have investigated the relationship of the aspect ratio to the downdraft and/or outflow speed (Wolfson, 1990; Proctor, 1989; Krueger and Wakimoto, 1985; etc.). In general, wider cores have been shown to produce stronger outflows while narrower cores produce weaker outflows given some constant core depth (at least equal or larger than the width) and constant vertical velocity.

For this examination of aspect ratio, we will assume that the downdraft speed is nearly the same for each storm on a given day and will simply compare the relative values of the aspect ratio of each storm with the relative values of outflow strength to determine if any relationship exists between the two. The reflectivity core will be defined as the region of 40 dBZ and greater and the aspect ratio of the core 2.5 - 5 minutes prior to surface outflow will be used.

3.4 *Analysis*

3.4.1 *Environmental conditions*

Figure 3.1 shows the sounding for August 18, 1992 from Orlando. This sounding is reasonably representative of all 3 days investigated in this study. The surface wind is from the SW at 3 m s^{-1} and the wind veers with height throughout the entire depth of the sounding, with winds becoming northerly around 500 mb and then northeasterly by 300 mb. Speeds increase slowly from 3 m s^{-1} at the surface to 10 m s^{-1} near 350 mb. The sounding is characterized by a well mixed layer from the surface to near 880 mb, which is roughly the height of both the convective condensation level (CCL, assumed to be height of cloud base of cumuliform clouds) and the lifted condensation level (LCL). Above this layer, the lapse rate is nearly moist adiabatic throughout the depth of the troposphere along the θ_w = 22 °C adiabat. The surface mixing ratio is 16.4 g kg^{-1} and above the mixed layer the dewpoint profile decreases at roughly the same rate as the temperature up to 450 mb, beyond which the atmosphere dries out more quickly. The nearly moist adiabatic lapse rate, combined with the mixed layer potential temperature and mixing ratio, produce a Convective Available Potential Energy (CAPE) of 697 J kg^{-1} as evidenced by the "small" surface based Lifted Index (LI) of -1.5 °C. Table 3.3 gives the thermodynamic parameters for the soundings from the three days investigated.

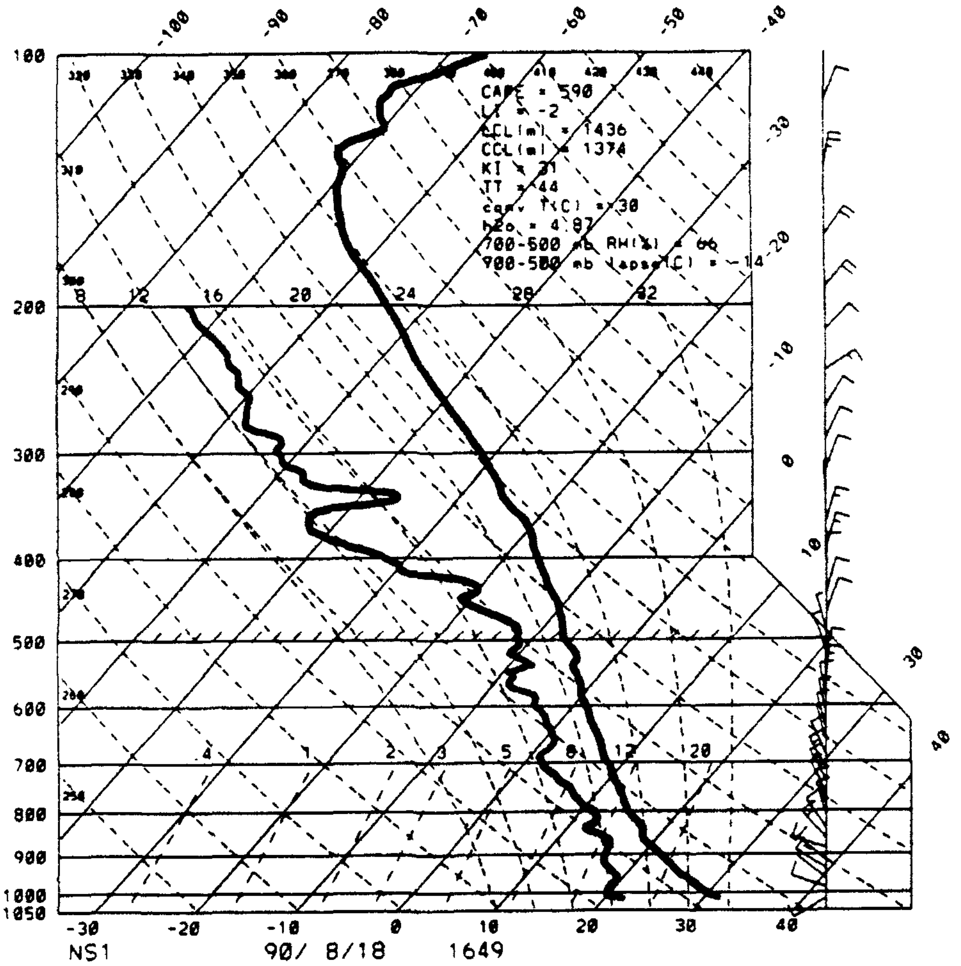

Figure 3.1 August 18, 1990 1649 UTC sounding for Orlando. On wind staffs, short barbs are 2.5 m s^{-1} and long barbs are 5 m s^{-1}.

Table 3.3 Sounding characteristics for the three soundings used in this study.

DATE	TIME (UTC)	L.I. (°C)	CAPE (J kg^{-1})	CCL (m)	LCL (m)	PRECIP. WATER (cm)	HT MELT LEVEL (m)
8-18	1649	-1.5	697	1366	1371	4.88	3929
8-21	1658	-1.7	776	1410	1399	5.05	4633
8-22	1653	-2.8	436	1378	1580	3.85	4721

3.4.2 *Assessment of Asymmetry*

To verify that the downbursts examined were not highly asymmetric and that the analyzed radial velocity data were representative of the downburst events, we compared the surface differential velocities from both FL-2C and UND for each downburst case. The differences between FL-2C and UND (Table 3.4) set a lower bound for asymmetry, that is, the asymmetry could be even worse based on a complete dual Doppler analysis, however we have no reason to believe it is.

Table 3.4 Comparison of FL-2C and UND surface ΔV's for the 8 downburst cases.

Case	FL-2C ΔV (m s^{-1})	UND ΔV (m s^{-1})
18A	12	13
18B	14	15
18C	10	10
18D	16	18
21A	10	15
21B	27	22
22A	30	26
22B	**	25

** - Not sampled by FL-2C

3.4.3 *Case investigations*

3.4.3.1 *Discussion of thunderstorm activity (August 18, 1990)*

At approximately 1830 a line of storms developed along a boundary which was most likely the eastern sea-breeze. These storms produced a large gust front (upper right corner) that began propagating WSW toward FL-2C around 1850 as shown in Figure 3.2a. At the same time, other cells began developing to the NNW at ~57 km from FL-2C. The plot of surface conditions in the mesonet shows that winds were light and variable, temperatures were 33-36 °C and dewpoint temperatures were generally between 22 and 25 °C. (Figure 3.3a).

At 1850, one cell had formed at 014/36 [azimuth (deg)/range (km)] (Figure 3.2b) and then decayed by 1907. At 1907, near 000/36 two distinct cells began to grow (Figure 3.2b). By 1912, the right cell (18A) dominated and eventually produced a downburst with a ΔV of 12 m s^{-1} at 1920. By this time, the original line of storms and the gust front had moved within 45 km of the radar.

The outflow from storm 18A moved SE from the storm to ~25 km NE of FL-2C. At 1927, storm 18B formed at 028/23 and by 1932 storm 18D formed at 020/24. By 1940 three more cells were detected by the radar, one of which was storm 18C located at 037/23 (Figure 3.2c).

By 1945, surface conditions within the mesonet had changed very little from 1850. However, north of the mesonet, surface outflow was detected by the radar from storm 18B just as the leading edge of the outflow from storm 18A had reached 18B. Only 2

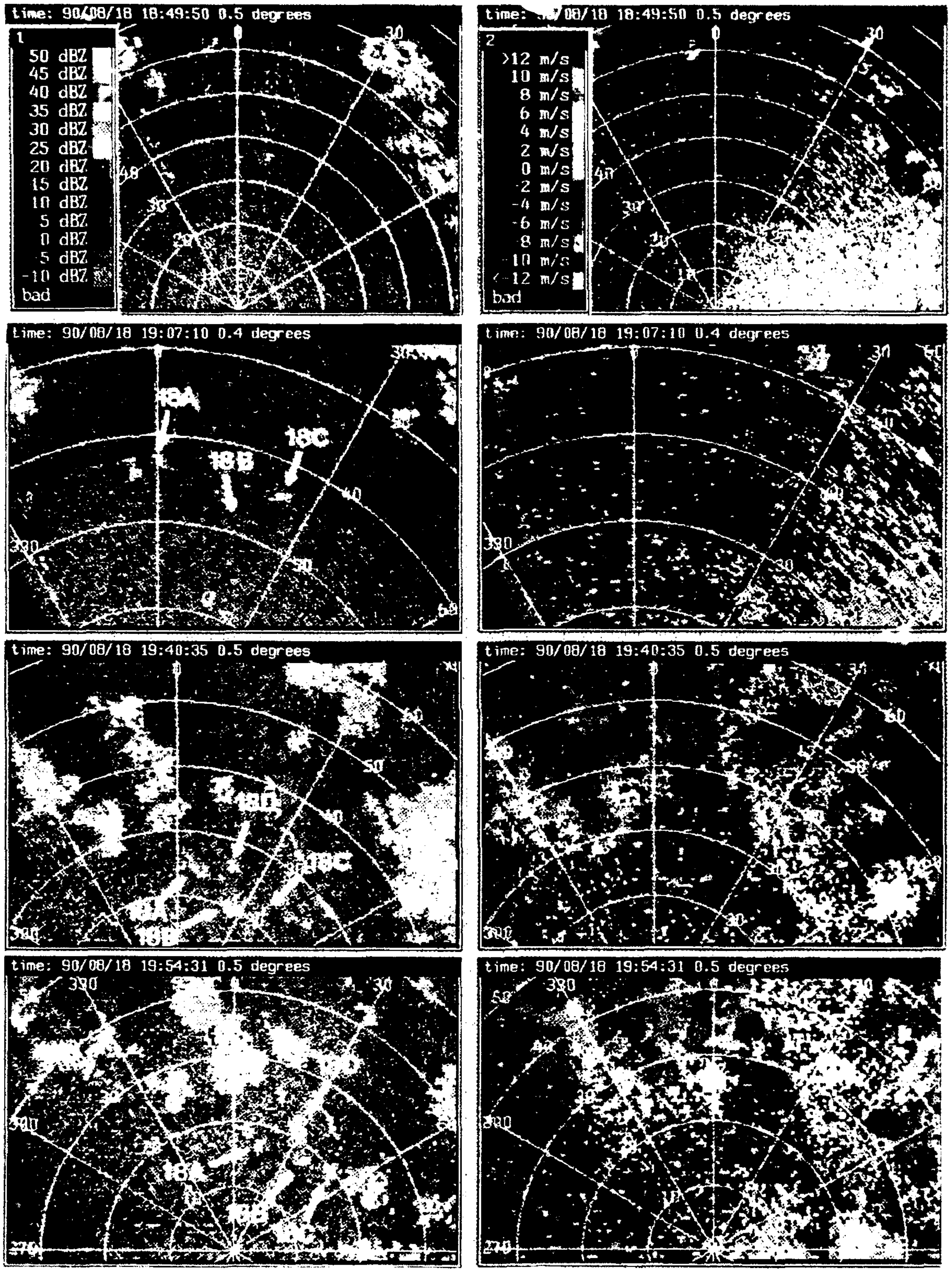

Figure 3.2 (left) Reflectivity and (right) velocity displays from FL-2C on August 18, 1990 at (a) 1850, (b) 1907, (c) 1940 and (d) 1954 UTC. Values are color coded according to the scales on the left edge of the first time plots.

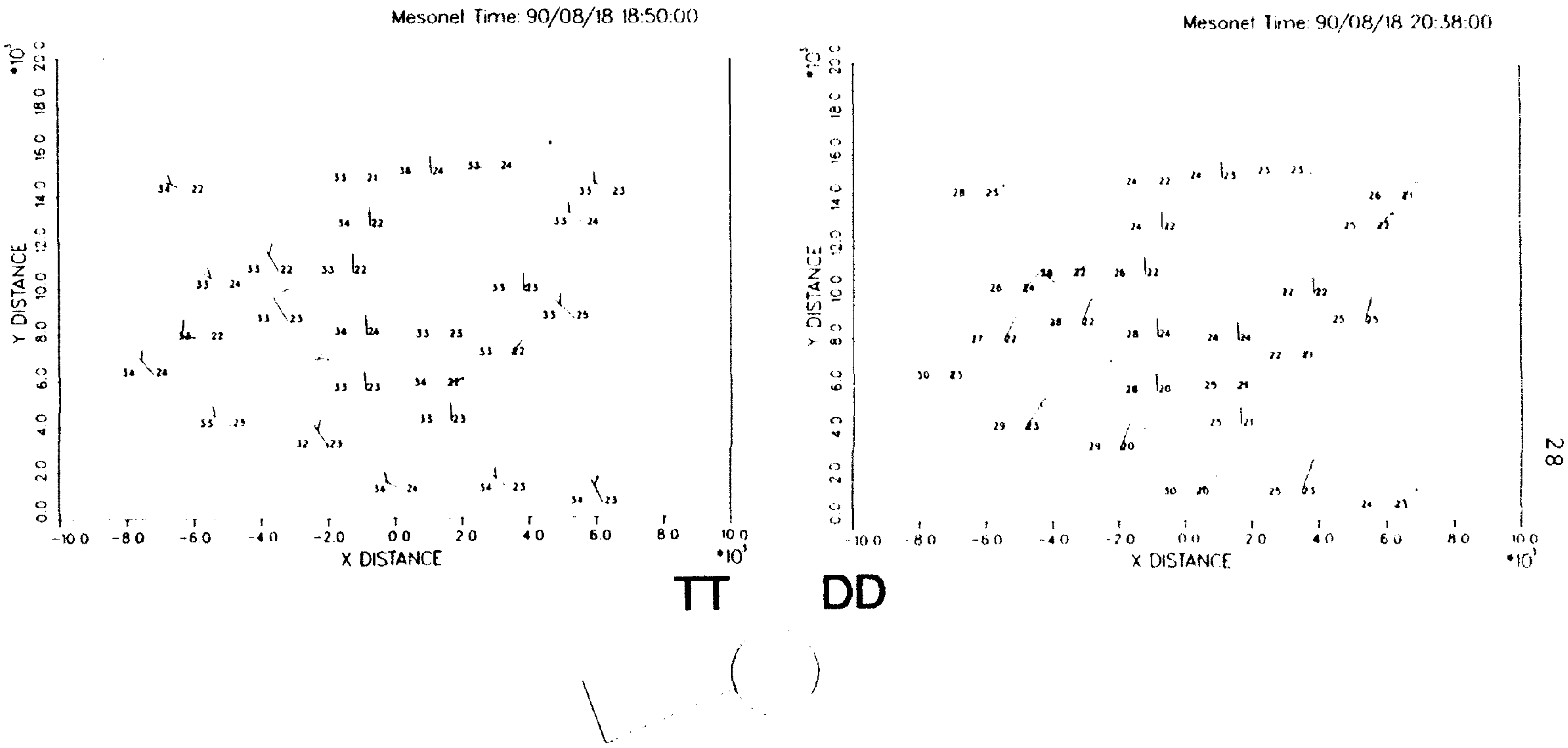

TT = Temperature (deg C)

DD = Dewpoint temperature (deg C)

Winds in m/s (long 5, short 2.5)

Figure 3.3 Plot of mesonet conditions at (a) 1850 and (b) 2038 UTC. Station model is shown under main figure. Distances are km from FL-2C.

minutes later, the outflow from 18B peaked at a ΔV of 12 m s^{-1}. At 1951, surface outflow from storm 18D was detected and reached a maximum velocity difference of 16 m s^{-1}. Storm 18C produced weak outflow (ΔV = 10 m s^{-1}) at 1955, just ahead of the large gust front that approached from the NE and overtook the storm (Figure 3.2d).

By 2010 the storms began merging with each other and the large gust front had entered the NE corner of the mesonet. The area remained a large conglomerate of reflectivity and propagated SW across the mesonet (Figure 3.3b) with time.

3.4.3.2 *Downbursts lifecycle structure (August 18, 1990)*

Analysis of the reflectivity field associated with storm 18A reveals a descending reflectivity core and a maximum storm mass of 4.0 x 10^{10} kg. Slantwise VIL calculations show an increase from 3.3 kg m^{-2} to 18.0 kg m^{-2} in only 5 minutes (1907-1912) and then a slight decrease at 1917 (Figure 3.4). This storm grew relatively quickly and was not very large (radar echo of only 2-3 km in diameter at the 0.5° elevation angle) and it produced a downburst with a ΔV of 12 ms^{-1} (the second strongest of the storms analyzed on the 18th).

The velocity field analysis reveals a local cyclonic rotation maximum ΔV of 8 m s^{-1} at a height of 1.8 km approximately 5 minutes prior to initial surface outflow and 17 minutes prior to maximum surface outflow. However, the rotation was nearly constant from the time it was first noted through the time of maximum surface outflow, unlike precursors examined in previous studies of Eilts and Oakland (1989) and Isaminger

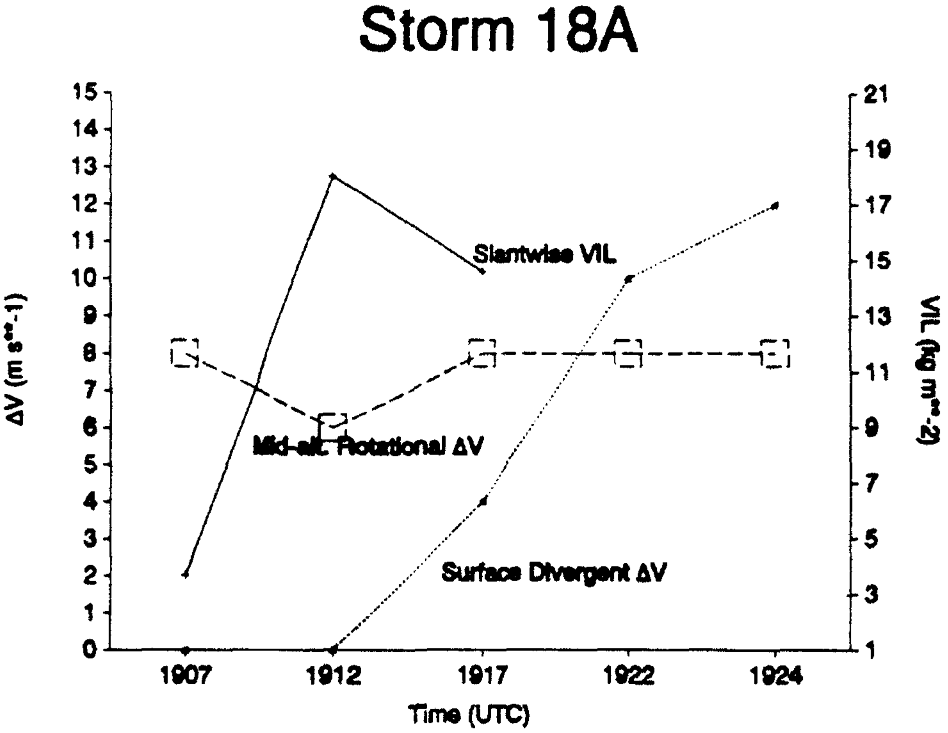

Figure 3.4 Time series of slantwise VIL, mid-altitude rotational ΔV and surface divergent ΔV for case 18A.

(1988), in which a distinct maximum was noted. Thus, the occurrence of the rotation may be considered a precursor, but the constant strength of the rotation does not seem to predict the observed increase in the surface outflow strength. Weak convergence was noted within the storm but was not considered further due to its sporadic nature in time and space.

Storm 18B also exhibited a descending reflectivity core (Figure 3.5) but the maximum storm mass was an order of magnitude smaller than that for 18A (Table 3.5). The slantwise VIL for 18B increased from 2.5 kg m^{-2} to a maximum of 7 kg m^{-2} at the

Table 3.5 Outflow strength precursors for the 8 downburst cases.

CASE	ΔV (m/s)	Slant-wise VIL max (J/kg^2)	Aspect Ratio (Z/L)	Storm Mass max (kg)	Max Surf. Ref. (dBZ)	Surf. based stable layer?	Con ΔV (m/s)	Rot ΔV (m/s)
18A	12	18	1.96	4.0×10^{10}	50	N	---	8
18B	12	7	2.25	3.3×10^{9}	50	Y	---	--
18C	10	10	1.50	3.3×10^{9}	50	Y	12	--
18D	16	10	1.21	8.3×10^{9}	50	N	8	--
21A	10	9	4.08	6.2×10^{9}	52	Y	---	12
21B	27	--	--	--	55	N	---	--
22A	30	24	1.92	6.3×10^{10}	50	Y	12	--
22B	25	18	1.51	1.9×10^{11}	50	N	---	8

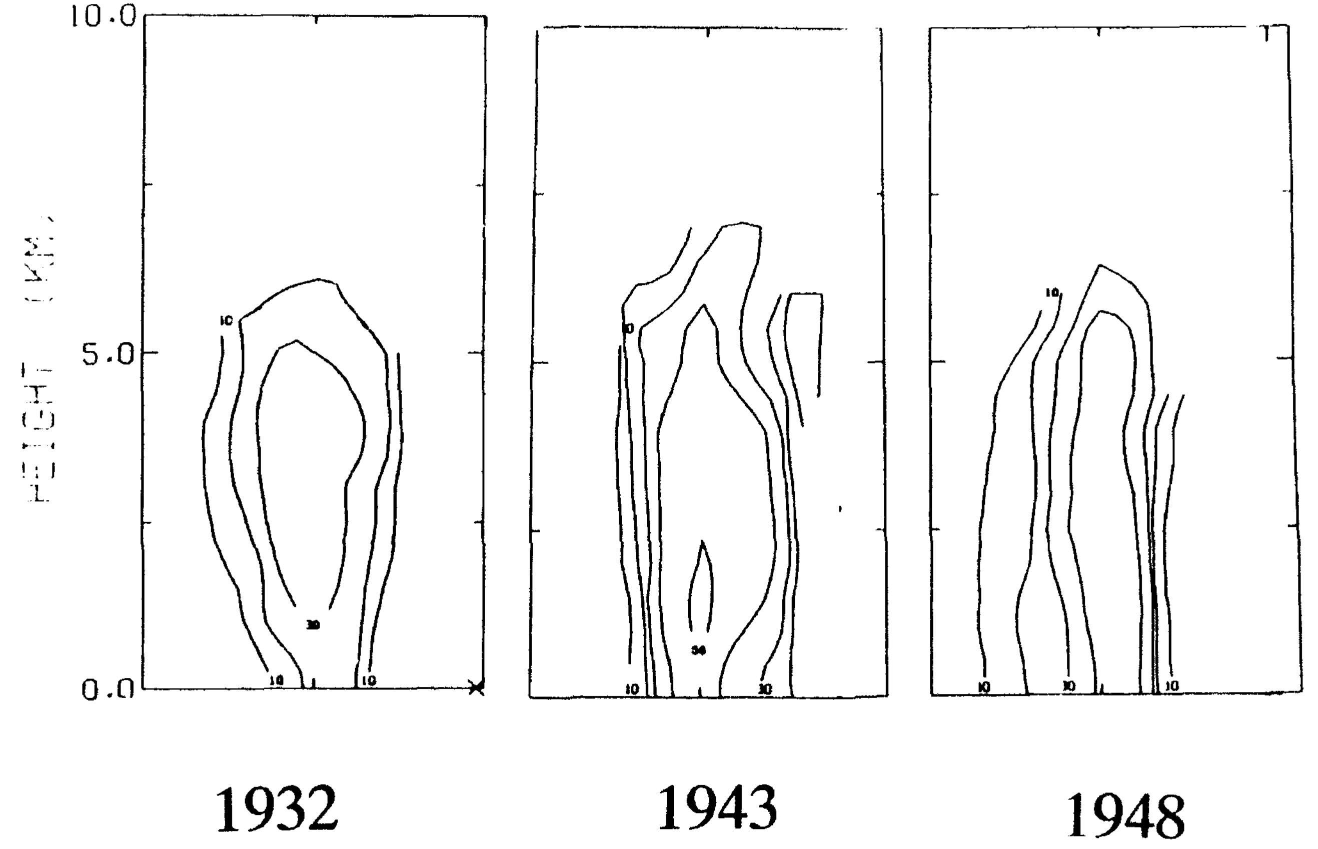

Figure 3.5 Vertical cross sections of reflectivity for case 18B at 1932, 1943 and 1948 UTC. Contours are shown every 10 dBZ from 10 to 50 dBZ.

time of initial surface outflow (Figure 3.6). This maximum was smaller than that for 18A but occurred 10 minutes prior to maximum outflow. This storm (18B) with smaller mass and slantwise VIL values than storm 18A produced the same strength outflow. The velocity field at mid-altitudes did not contain any convergence or rotation above the chosen threshold (Figure 3.6).

Storm 18C produced the weakest outflow of the four storms investigated from August 18, reaching a maximum of only 10 m s^{-1}. This storm did produce a descending reflectivity core like the other storms on this day (Figure 3.7). The slantwise VIL peaked at 12.8 kg m^{-2} (Table 3.5) twelve minutes prior to the maximum in the surface ΔV, but did not drop off as rapidly as in 18A and 18B (Figure 3.8). The storm mass reached a maximum of 3.3 x 10^9 kg (the same value as for 18B). Storms 18B and 18C were very similar in size (Figure 3.2d) but 18C's outflow was slightly weaker (10 m s^{-1}).

The velocity field contained mid-altitude convergence that was first noted at nearly the same time as the initial surface divergence. The convergence decreased, then increased to a ΔV maximum of 12 m s^{-1} only 4 minutes prior to maximum surface outflow (Figure 3.8). Rotation was noted within the storm but only sporadically and thus was not considered further.

Storm 18D was the largest in low-altitude area of the storms analyzed on this date, produced the strongest outflow (ΔV of 16 m s^{-1}) and had a descending core (Figure 3.9). The slantwise VIL for 18D is not the largest of the cases from this date, reaching a

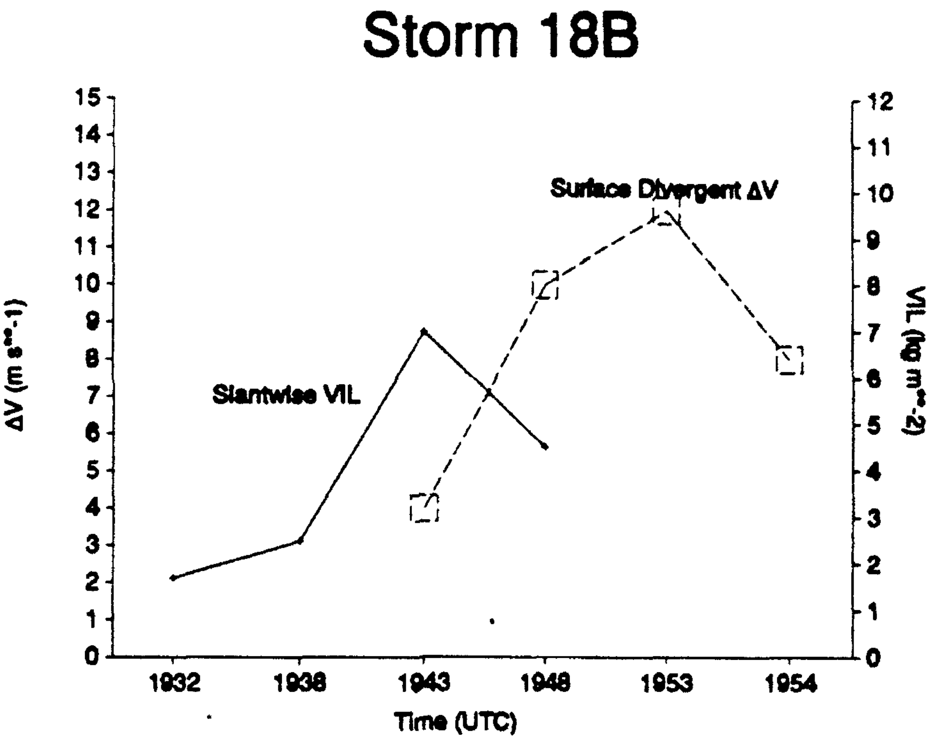

Figure 3.6 Time series of slantwise VIL and surface divergent ΔV for case 18B.

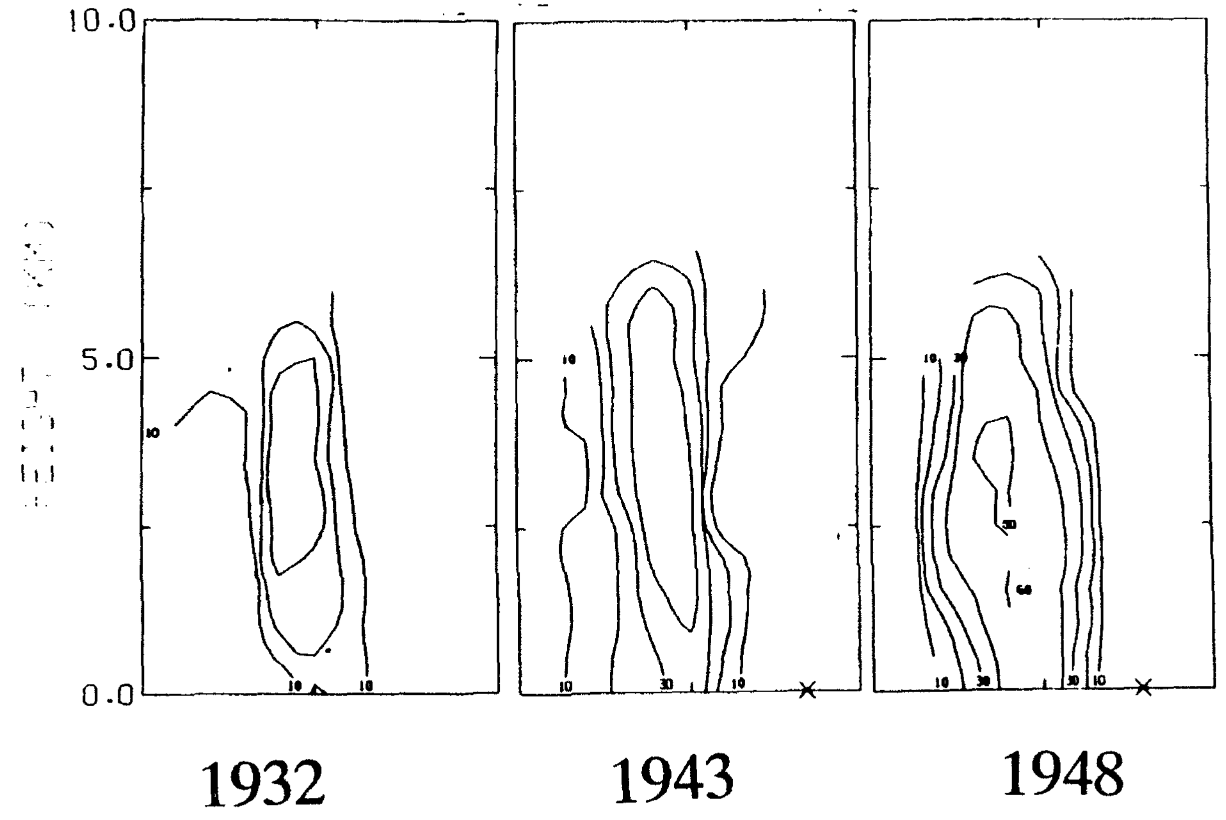

Figure 3.7 Vertical cross-sections of reflectivity for case 18C at 1932, 1943 and 1948 UTC. Contours are shown every 10 dBZ from 10 to 50 dBZ.

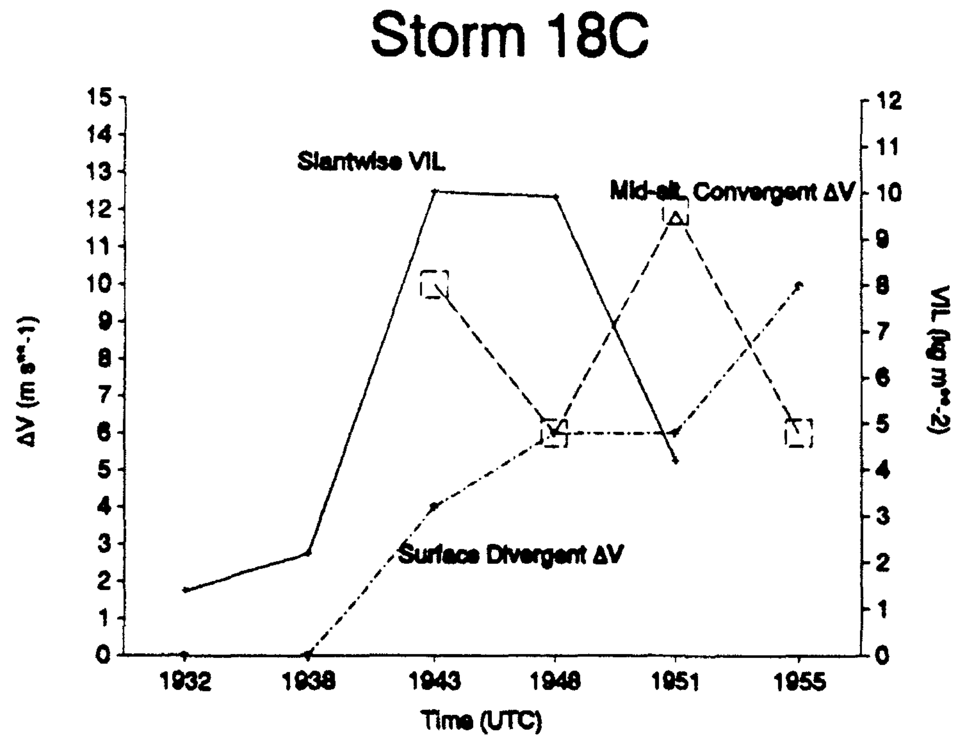

Figure 3.8 Time series of slantwise VIL, mid-altitude convergent ΔV and surface divergent ΔV for case 18C.

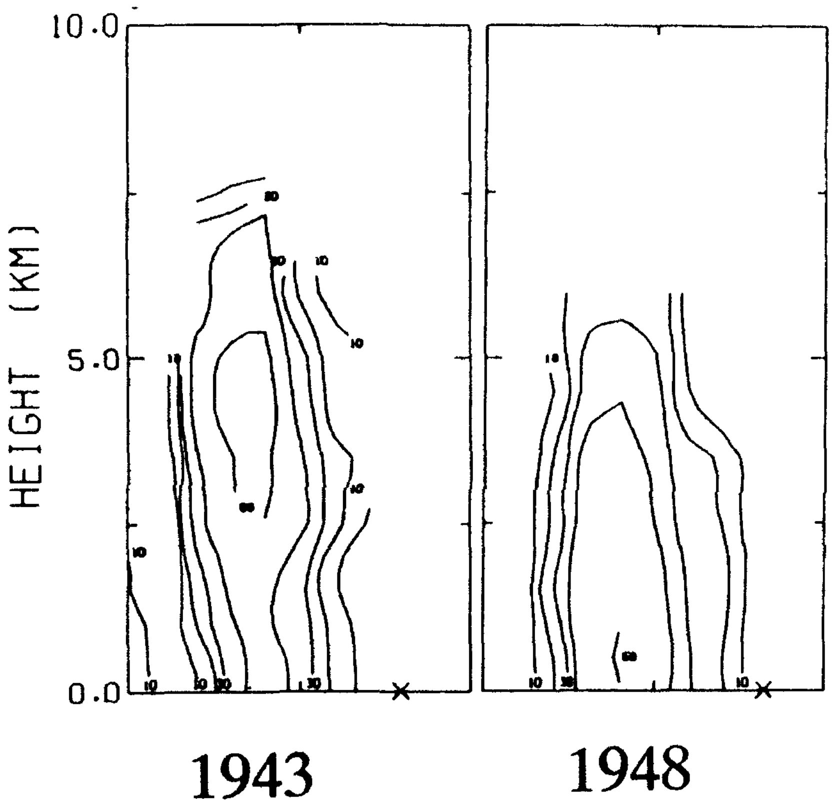

1943 1948

Figure 3.9 Vertical cross section of reflectivity for case 18D at 1943 and 1948 UTC. Contours are shown every 10 dBZ from 10 to 50 dBZ.

maximum of only 10 kg m^{-2} three minutes prior to initial surface outflow and 6 minutes prior to maximum surface ΔV. Maximum storm mass was 8.3×10^{9} kg which is smaller than 18A (the largest mass storm of the 18th storms). The velocity field exhibited only weak mid-altitude convergence ΔV's of 6 to 8 m s^{-1}, but like 18A did not show a distinct peak (Figure 3.10).

The observed surface outflow variability in the four August 18th storms does not appear to be explainable by differences in the observed velocity and reflectivity fields nor, does it appear possible that the differences could predict the variability. The storms all developed ahead of a very strong gust front and were similar in size and reflectivity structure. None of the storms produced severe downbursts, though differences in the outflow strengths were detectable. Examination of the upper altitude velocity fields does not suggest which storms would be strongest. In fact, the strongest surface outflow was associated with the weakest "velocity precursor" and the second strongest outflow storm had no mid-altitude velocity feature above the 4 m s^{-1} threshold. In addition, there was no consistency in the features observed; two storms had convergence and one had rotation.

The reflectivity structure of the four storms did not reveal any definitive explanations for the variability either. The maximum storm mass values were all within one order of magnitude of each other for the four 18th storms with 18A having the largest value but producing only the second strongest outflow. The aspect ratio for the four August 18th storms varied from 1.21 to 2.25 (Table 3.4) with the widest core producing

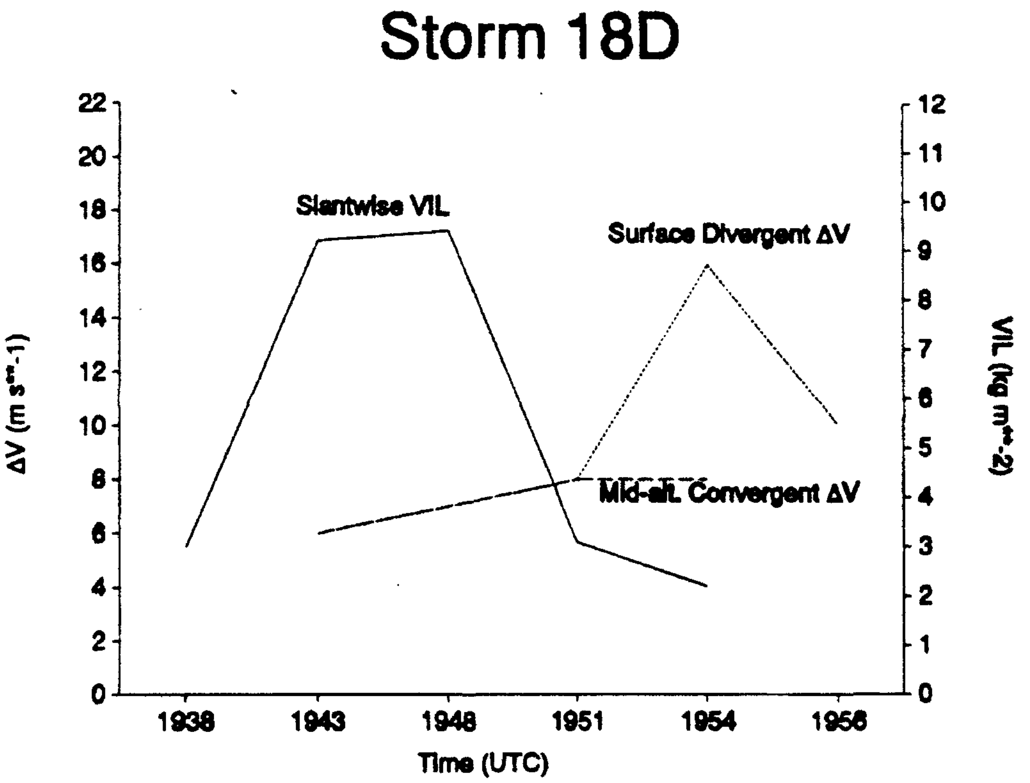

Figure 3.10 Time series of slantwise VIL, mid-altitude convergent ΔV and surface divergent ΔV for case 18D.

the strongest outflow, but the narrowest core did not produce the weakest outflow. The is only vaguely consistent with other's results (Krueger and Wakimoto, 1985). The trend in slantwise VIL calculations did give some indication of the timing of an increase in a storm's outflow ΔV.

3.4.3.3 *Discussion of thunderstorm activity (August 21, 1990)*

At 2130 a cluster of storms was located from 355/45 to 015/37 and a gust front was propagating from these storms toward the southwest (Figure 3.11a). At this time the conditions within the mesonet were fairly uniform with temperatures ranging from 33°C to 35°C, dewpoints generally between 22 and 25 °C, and winds light from the southwest through southeast (Figure 3.12a).

By 2153, storm 21A began to form just ahead of the gust front at 348/30 (Figure 3.11b) and storm 21B was first noted at 2154, although the latter was well developed and slightly larger than 21A. At this time, storm 21B was located outside the FL-2C scanning sector. At 2156, storm 21A was primarily located behind the reflectivity thin line and wind shift line associated with the gust front and surface outflow that was detected from another storm. Storm 21A reached a peak in surface divergence ΔV ($10\ m\ s^{-1}$) at 2200, but continued to produce weak ($< 8\ m\ s^{-1}$) surface outflow until 2209 even though the storm remained in apparently cooler surface conditions.

At 2159, storm 21B was producing surface outflow with a ΔV of $18\ m\ s^{-1}$ and was

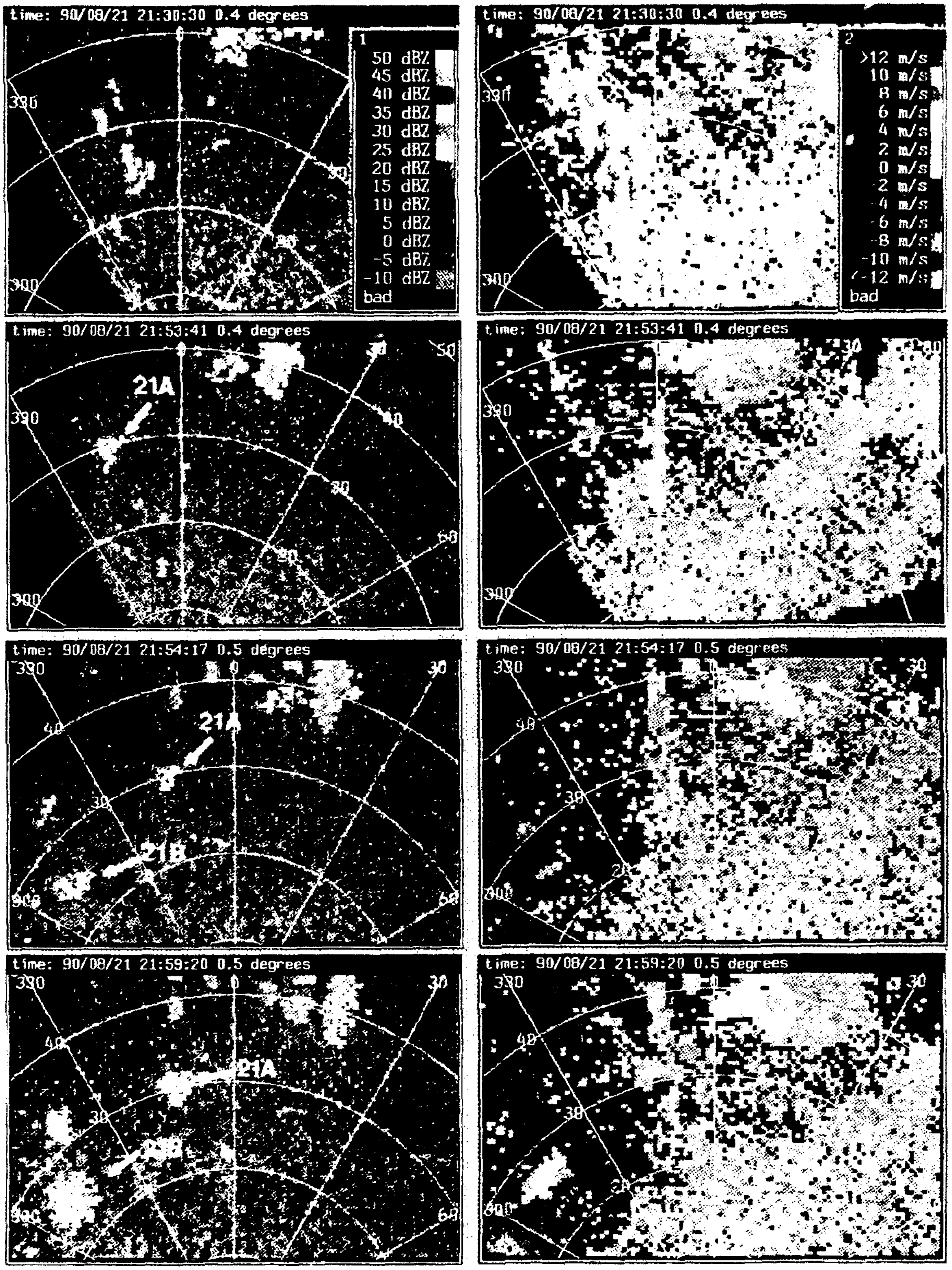

Figure 3.11 (left) Reflectivity and (right) velocity displays from FL-2C on August 21, 1990 at (a) 2130, (b) 2153, (c) 2154 and (d) 2159 UTC. Values are color coded according to the scale on the left edge of the first time plots.

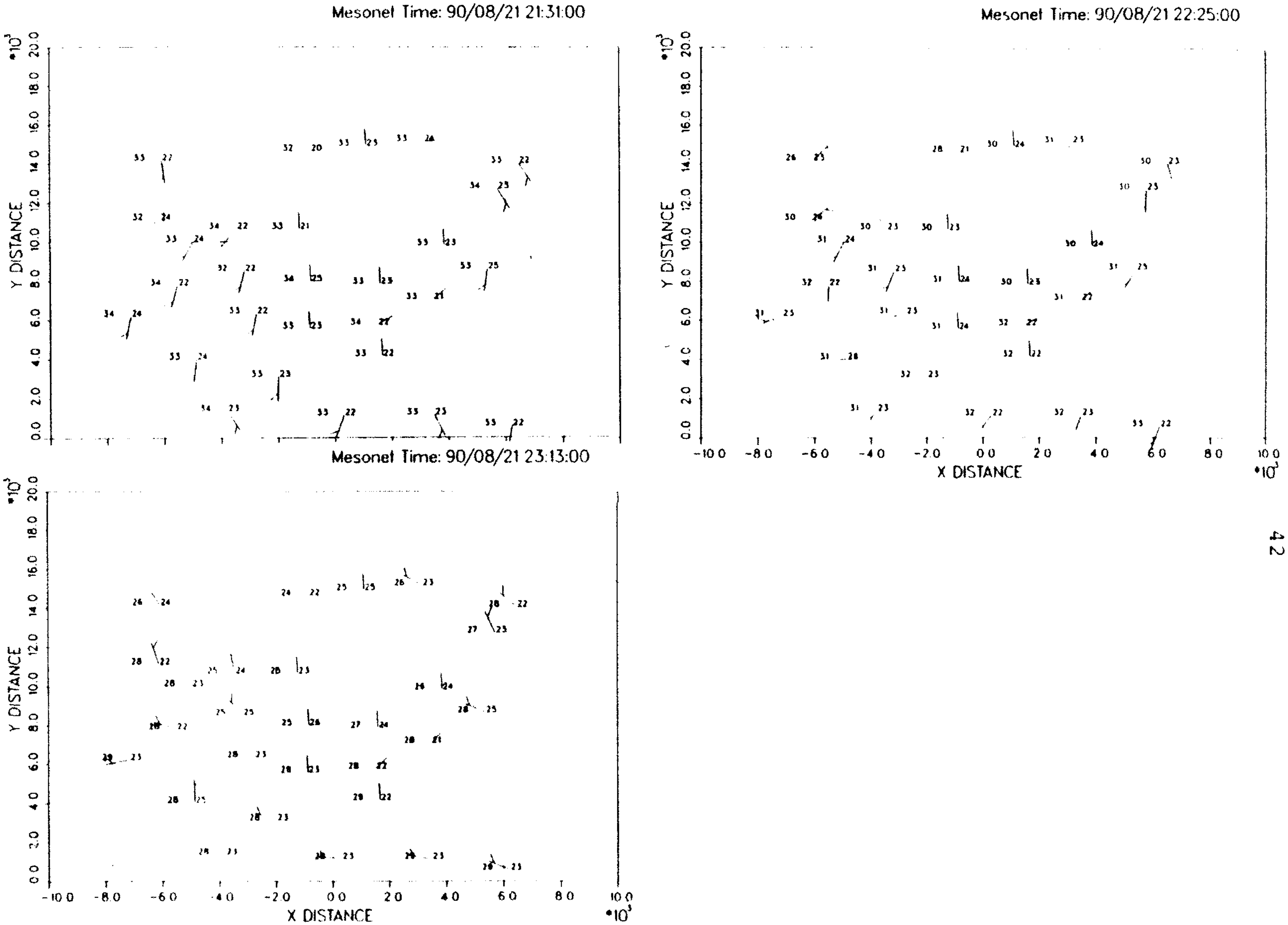

Figure 3.12 Surface mesonet conditions for August 21, 1990 at (a) 2130, (b) 2225 UTC and (c) 2313 UTC.

moving closer to the FL-2C scanning sector (Figure 3.11c). Storm 21B continued to move ENE and eventually moved into the sector where it produced a maximum ΔV of 27 m s^{-1} at 2218. Around 2225 the downburst outflow began to penetrate the mesonet as surface temperatures fell and dewpoints remained fairly constant (Figure 3.12b). By 2313, the outflow had propagated across the entire mesonet and temperatures ranged from 25°C to 29°C and dewpoints ranged from 22 to 25 °C. Winds had also veered behind the gust front and were generally westerly (Figure 3.12c).

3.4.3.4 *Downbursts lifecycle structure (August 21, 1990)*

Analysis of the reflectivity of storm 21A revealed a descending reflectivity core (Figure 3.13) ~10 min before the downburst began and a maximum storm mass of 6.2 x 10^9 kg (similar to the 18th storms). Slantwise VIL values increased from 3 kg m^{-2} to 9.2 kg m^{-2} in the five minutes prior to surface outflow and then decreased during the time of maximum surface ΔV (Figure 3.14). The aspect ratio (Table 3.4) was much higher for 21A than for the other storms in this study. No comparison with 21B can be made since 21B was not adequately sampled by the radar to determine a core aspect ratio. 21A developed ahead of a gust front in a manner similar to the storms on August 18th and was similar in size as well. The outflow initially was ahead of the windshift line of the gust front but did not peak in strength until the gust front had undercut the storm. Analysis of the velocity field indicated that rotation was the dominant feature at mid-altitude; it reached a maximum ΔV of 12 m s^{-1} three minutes prior to the maximum in the

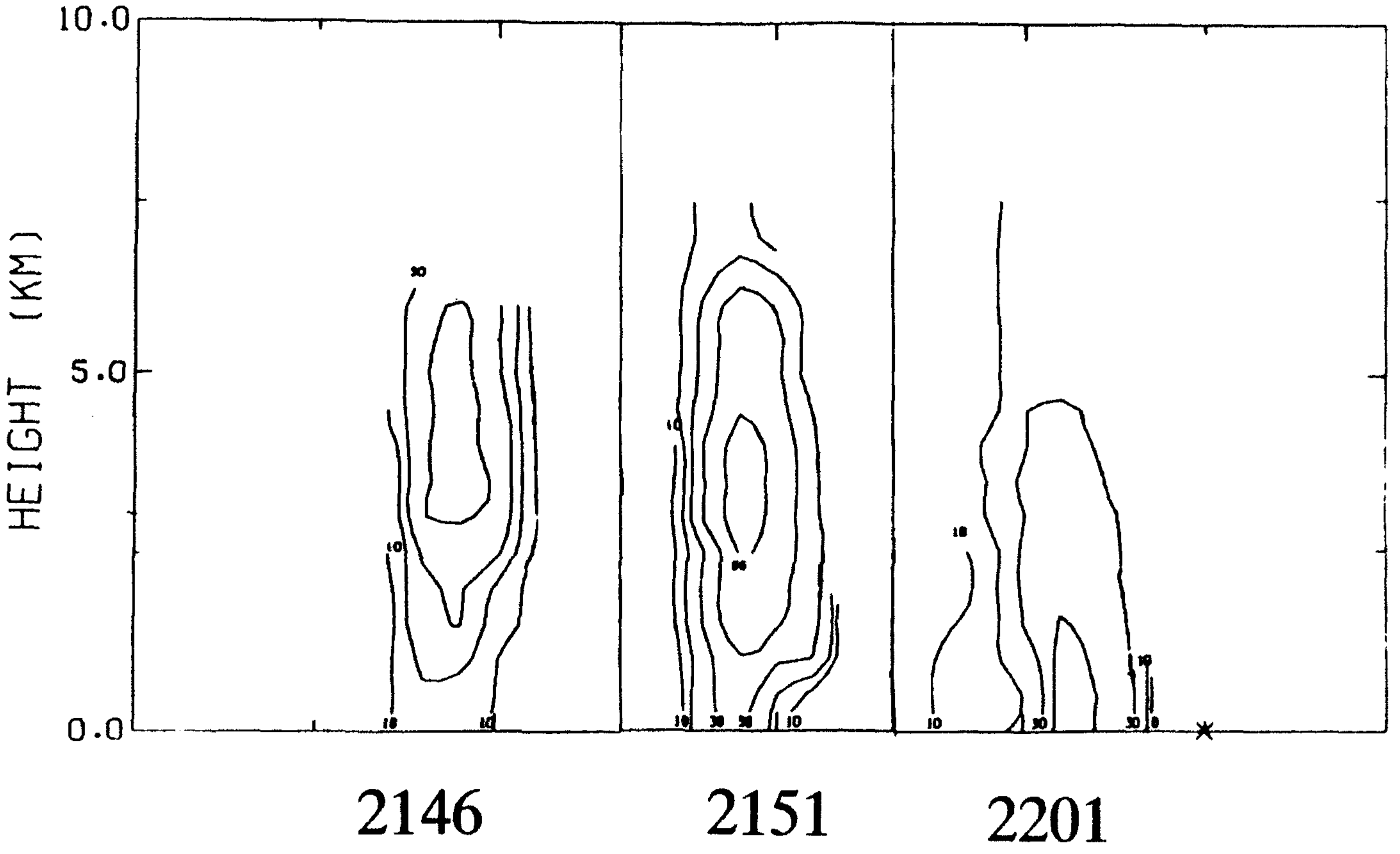

Figure 3.13 Vertical cross-section of reflectivity for storm 21A at 2146, 2151 and 2201 UTC. Contours are shown every 10 dBZ from 10 to 50 dBZ.

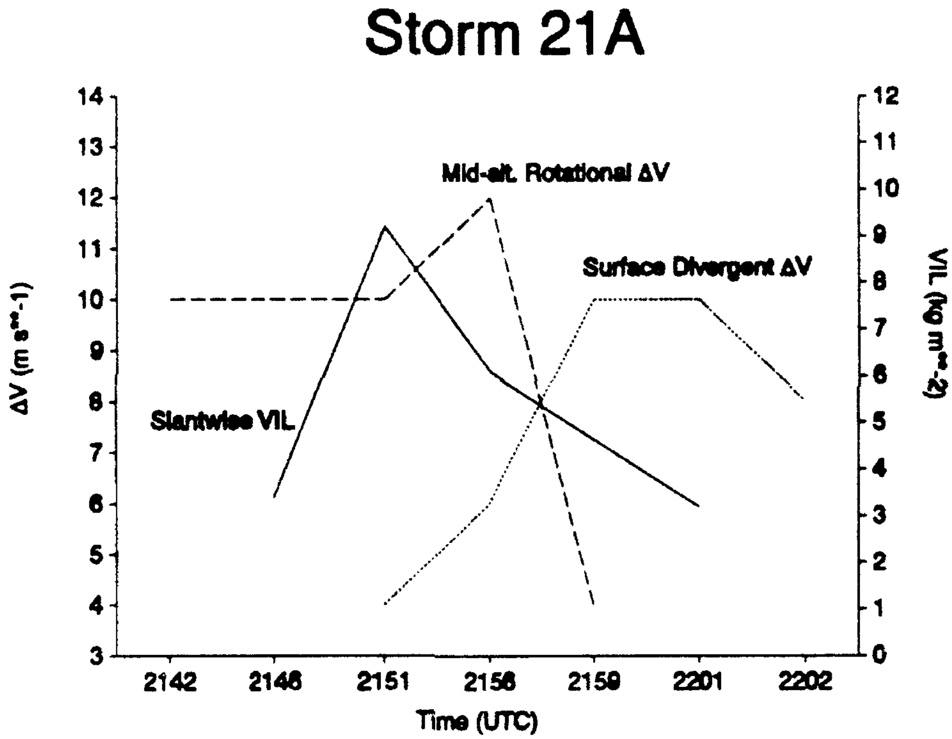

Figure 3.14 Time series of slantwise VIL, mid-altitude rotational and surface divergent for storm 21A.

surface outflow. The rotation ΔV decreased dramatically to only 4 m s^{-1} at the time of the surface maximum. This distinct maximum is more consistent with the findings of Eilts and Oakland (1989) and Isaminger (1988) than the storms of August 18th.

Storm 21B did not develop within the scanning sector of FL-2C and thus only low-level scans were available for this storm. Therefore, little comparison can be made between storms 21A and 21B except that 21B was considerably larger (Figure 3.11d) and its outflow considerably stronger. However, from only the low-level scans, it is clear that storm 21A was undercut by outflow from another storm and may have actually developed on the extreme edge of that outflow. The outflow from 21A persisted, although weakly (< 8 m s^{-1}), for nearly 10 minutes after reaching a maximum. Storm 21B did not appear to be affected or undergo any interaction with outflows from other storms. This raises the question: what effect did the outflow from another storm have on storm 21A? Since the outflow did persist for a while after reaching a maximum, would it have been stronger if it had not been undercut by another outflow?

3.4.3.5 *Discussion of thunderstorm activity (August 22, 1990)*

At 2000 storm 22B was detected at 280/35 in an apparently undisturbed environment as no boundaries were observed in the vicinity (Figure 3.15a). At this time surface winds within the mesonet were light and generally from the southwest, temperatures ranged from 34°C to 36°C, and dewpoints ranged from 18 to 22°C (Figure 3.16a). By 2036 storm 22B had grown significantly larger, the surface outflow had

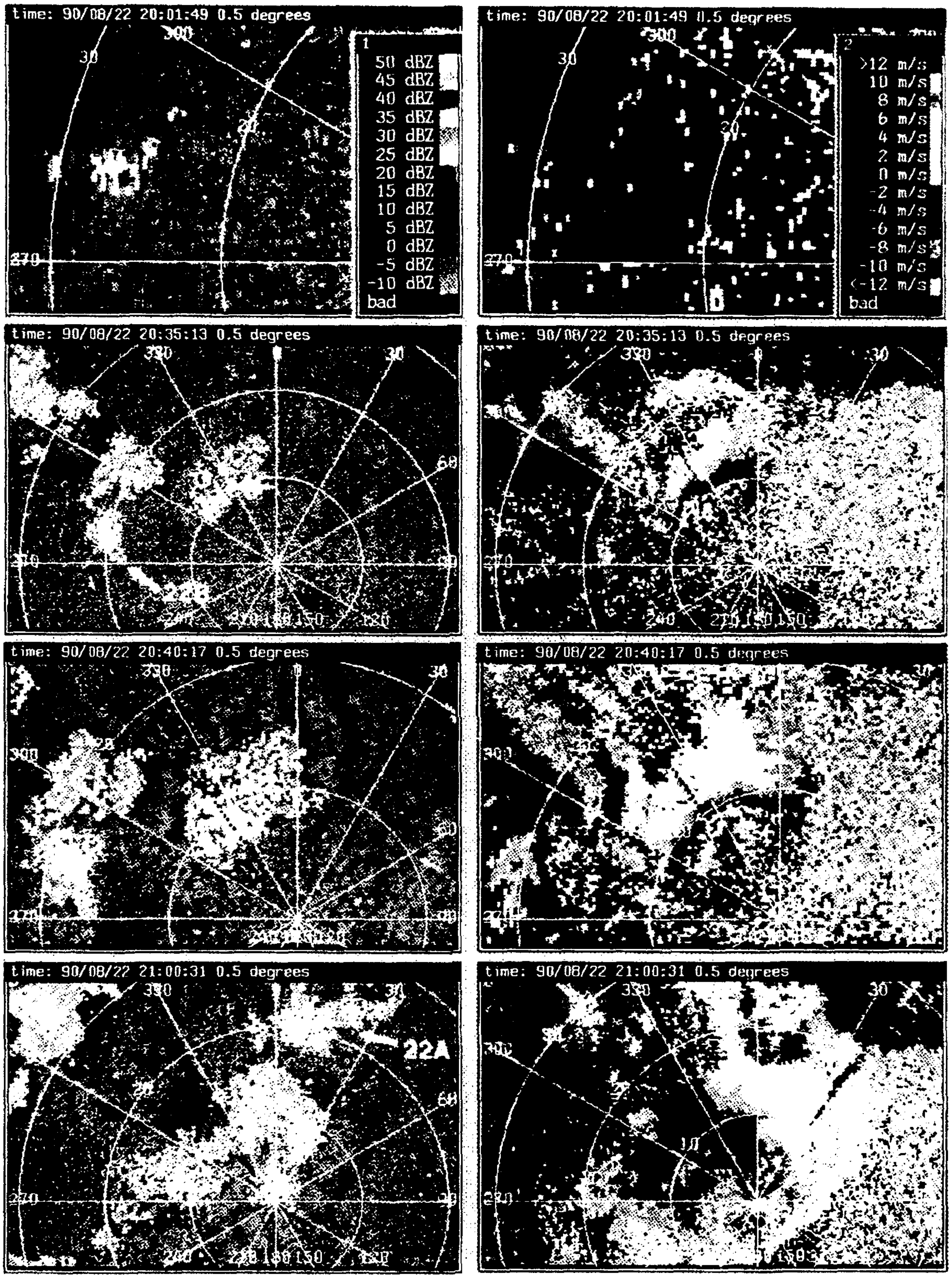

Figure 3.15 (left) Reflectivity and (right) velocity displays from UND for August 22, 1990 at (a) 2000, (b) 2035, (c) 2040 and (d) 2100 UTC. Values are color coded according to the scale on the left edge of the first time plots.

increased to a ΔV of 24 m s^{-1}, and a reflectivity thin line was associated with the eastward moving portion of the outflow. By 2042 the storm had produced its peak outflow ΔV of 25 m s^{-1}. As outflow reached the mesonet at 2040, cooler moister air moved into the western side (Figure 3.16b) and propagated across the entire mesonet with the leading edge exiting the mesonet around 2110.

At 2040 a convergence line, caused by outflow from 22B (located at 345/12), was positioned 20 km north of FL-2C (Figure 3.15c). By 2045 storm 22A began forming along the convergence line and by 2050 surface outflow was detected to the south of the convergence line (well within the outflow from storm 22B). By 2100 storm 22A had grown considerably larger and the peak in surface divergence ΔV (30 m s^{-1}) was reached (Figure 3.15d).

3.4.3.6 *Downbursts lifecycle structure (August 22, 1990)*

Storm 22A exhibited a descending reflectivity core as with other storms in the study (Figure 3.17) and had a maximum storm mass of 6.3×10^{10} kg, a value larger than any of the other storms investigated. The slantwise VIL values for this storm were much higher than those from the other days in the study with a maximum of 24.8 kg m^{-2} occurring 6 minutes prior to initial surface outflow and 18 minutes prior to the peak surface ΔV of 30 m s^{-1} which was also the strongest outflow observed in this study (Figure 3.18). Analysis of the velocity field of storm 22A revealed a mid-altitude convergence feature that peaked at 12 m s^{-1} at the time of initial surface outflow and 12

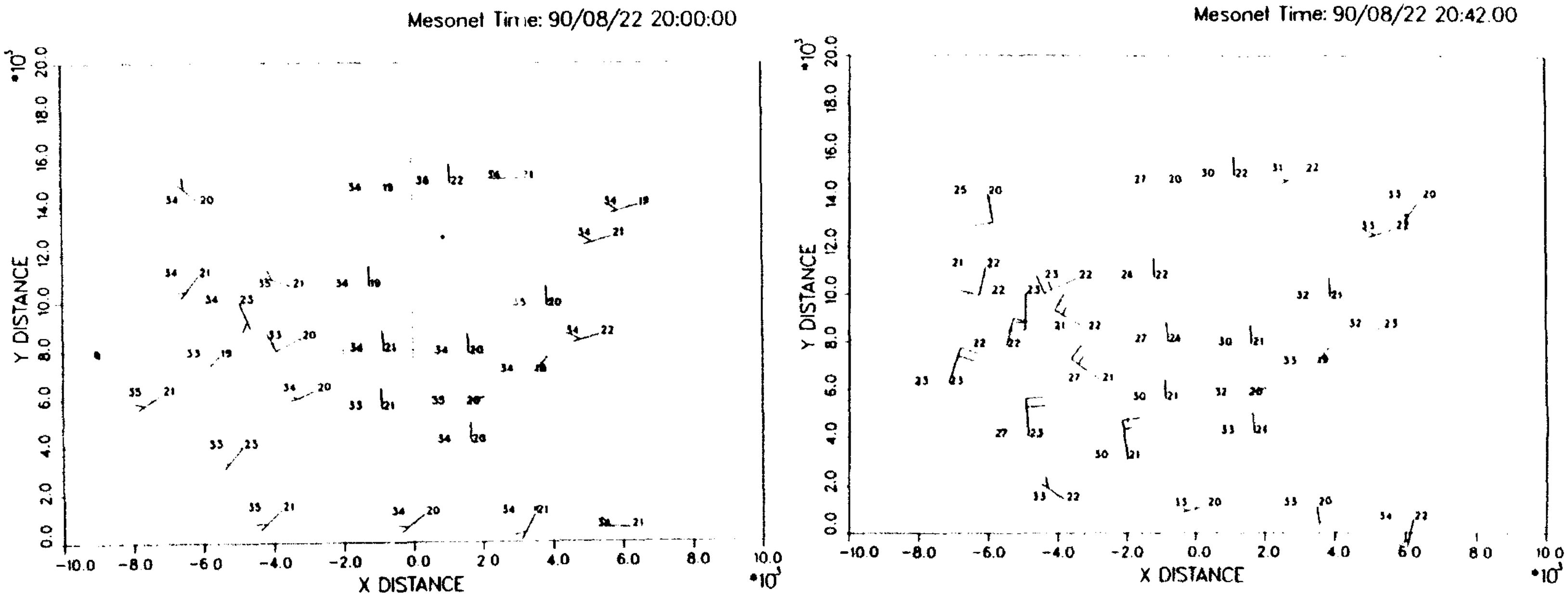

Figure 3.16 Surface mesonet conditions for August 22, 1990 at (a) 2000 and (b) 2042 UTC.

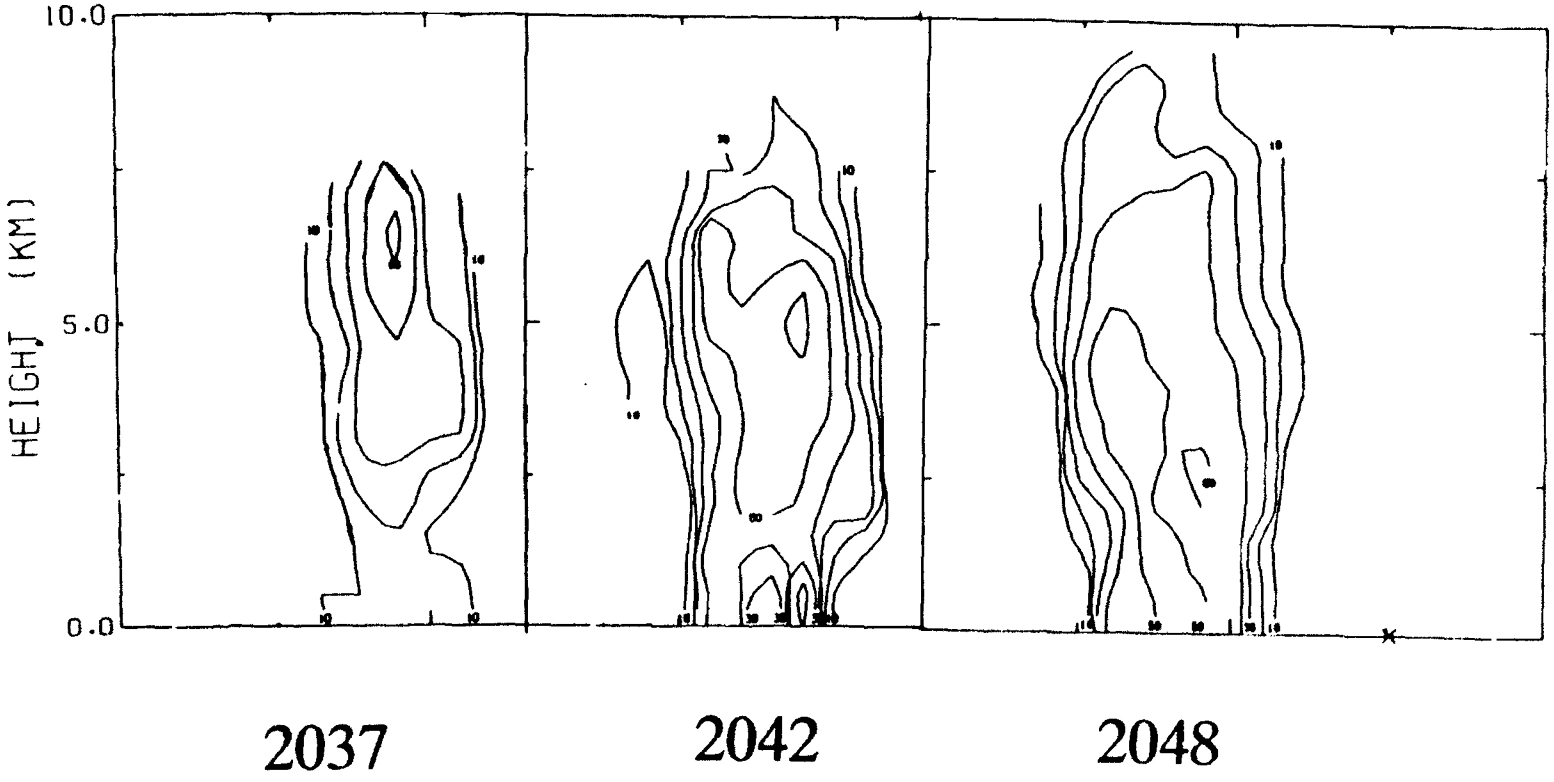

Figure 3.17 Vertical cross-section of reflectivity for storm 22A at 2037, 2042 and 2048 UTC. Contours are shown every 10 dBZ from 10 to 50 dBZ.

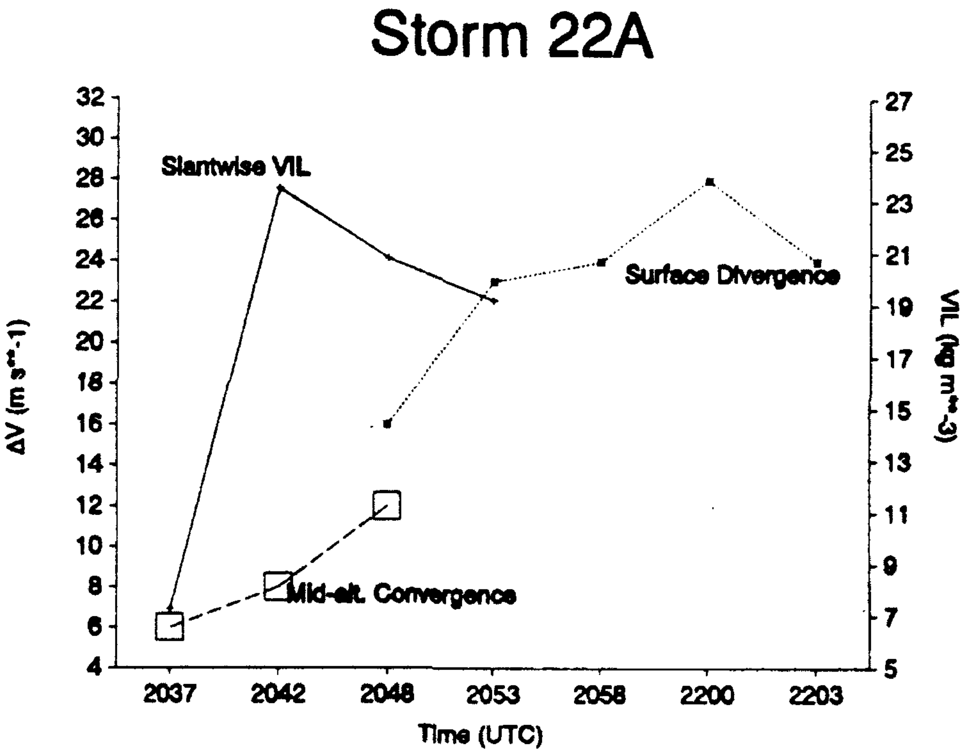

Figure 3.18 Time series of slantwise VIL, mid-altitude convergent ΔV and surface divergent ΔV for storm 22A.

minutes prior to the maximum at the surface.

Storm 22B exhibited a descending reflectivity core (Figure 3.19) and had a maximum mass of 1.9 x 10^{11} kg. This mass is the largest value of all the storms in the study. Slantwise VIL values for 22B peaked at the time of initial surface divergence and decreased significantly through the time of peak outflow (Figure 3.20). The VIL values themselves were less than those of 22A. This storm (22B) actually produced several pulses of outflow with the strongest one being considered here. This fact does raise some question as to the validity of comparing 22A and 22B since it appears that the storms had different dynamical forcings. However, the sizes and vertical structure are very similar for the two storms as can be seen in the two cross-sections.

Analysis of the velocity field for 22B revealed that mid-altitude rotation was the dominant feature but as in 22A the ΔV's were only 12 ms^{-1}. The rotation ΔV was noted as 12 m s^{-1} for ~4 minutes but they fell off to only 8 m s^{-1} during the time of initial outflow.

22A and 22B had outflows that were comparable in strength to that of 21B and had some similarities in the reflectivity structure. The core aspect ratios for the 22nd's storms were somewhat similar to each other, with the narrower core producing stronger outflow, contrary to previous studies. However the storms of August 22 had some differences, in that 22A's downdraft fell into what appears to have been a cool outflow from another storm and 22B was a "pulsing" type storm. 22A had a mid-altitude convergent velocity feature and 22B had a rotational velocity feature. The strength of

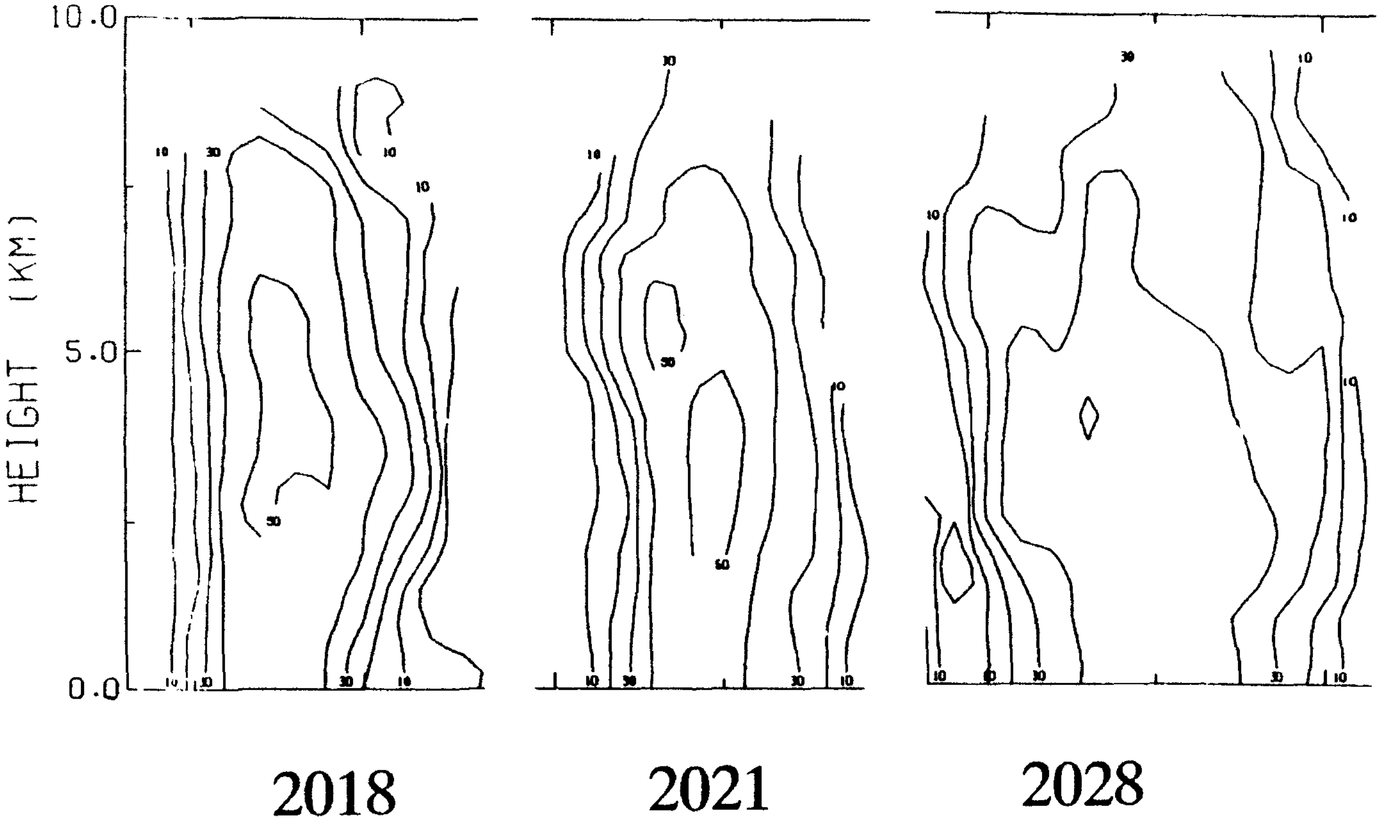

Figure 3.19 Vertical cross section of reflectivity for storm 22B at 2018, 2021 and 2028 UTC. Contours are shown every 10 dBZ from 10 to 50 dBZ.

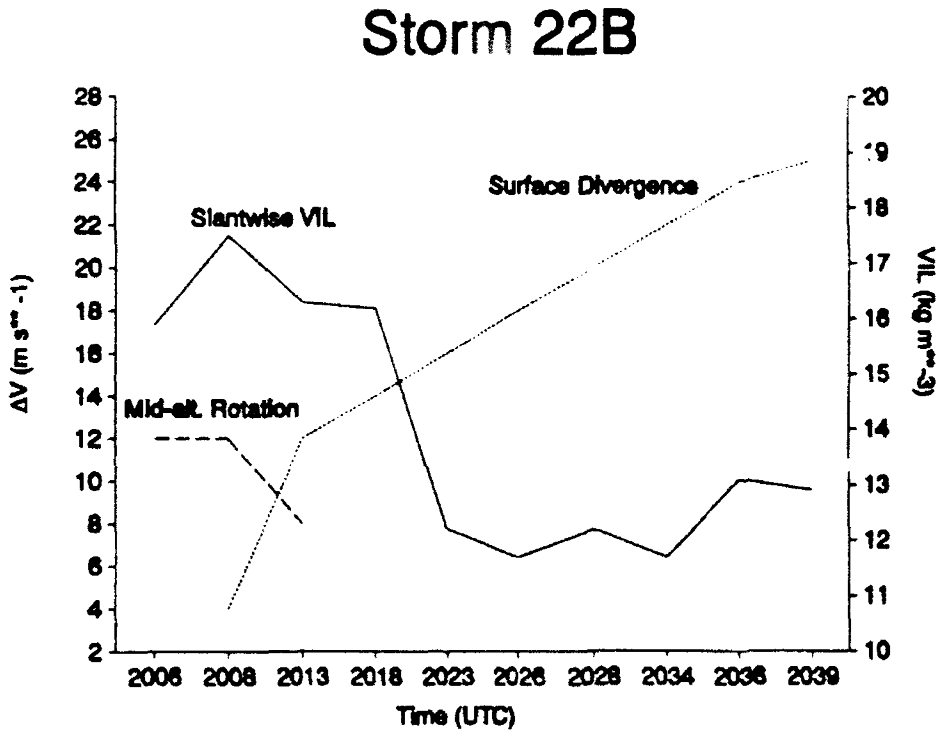

Figure 3.20 Time series of slantwise VIL, mid-altitude rotational ΔV, and surface divergent ΔV for storm 22B.

these features and their trends do not give any indication of the strength of the outflow. While storm 22A was undercut by another outflow, its outflow was still slightly stronger than that of 22B. Would 22A have been even stronger had it not been undercut?

3.5 *Motivation for additional investigation*

As can be seen from the foregoing discussion, the limited number of cases and data sources did not reveal any definitive answers concerning the cause of variability observed in the strength of Florida downburst surface outflows. The slantwise VIL trends showed a peak prior to the maximum in outflow strength for all the storms investigated. There also was some correlation in the maximum storm mass to the outflow strength. The strongest outflows (22A and 22B) had higher mass values than the weaker storms but nothing could be drawn from comparing individual storms. Aspect ratio values did not give any indication which storms would produce stronger outflows. However, one aspect of the storms that appears to warrant further consideration is the possibility that a downdraft falls into an existing outflow, which could have a damping effect (through dispersion of energy by gravity waves), on the outflow strength and thus diminish the potential strength of a downburst. Table 3.5 shows which storm outflows appear to have been affected by a ground-based stable layer caused by outflow from other storms. The similarity in storms and difference in results can be seen in the direct comparison of storms 21A and 21B (Figure 3.21). The maximum surface reflectivity for the two storms show that 21B's reflectivity was slightly higher and remained high for slightly longer.

However, these differences are small compared to the differences in the outflow strength.

We will investigate the effect of stable layers on outflow strength further in Chapter 4.

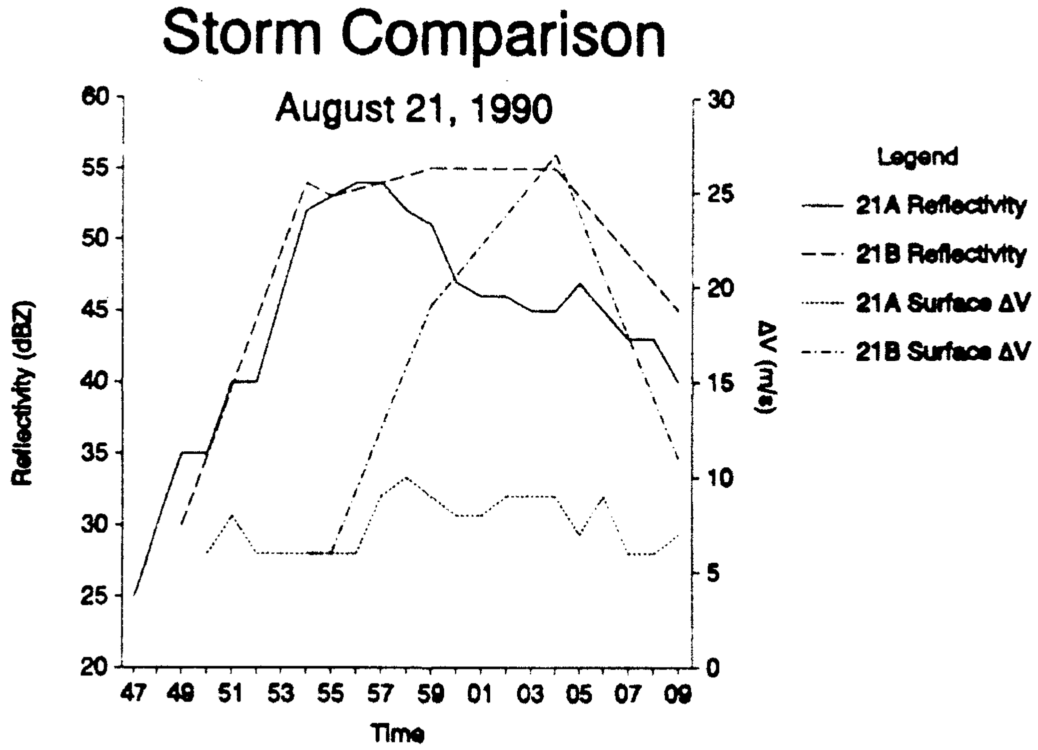

Figure 3.21 Comparison of maximum surface reflectivity and surface outflow ΔV for storms 21A and 21B (21A's outflow apparently impacted a previous outflow induced stable layer). Legend in upper right distinguishes the curves.

CHAPTER IV

MODELING STUDY

4.1 *Objective*

In this portion of the study we use the soundings from the three days investigated in Chapter III to numerically simulate three storms. We do a comparison of the microphysical structure of each simulated storm to determine if differences exist and if the differences can possibly explain the observed variability in outflow strengths. Further, we simulate three storms above different strength stable layers to investigate the effect of a downdraft falling into an existing outflow as was suspected as a possible reason for the observed variability.

4.2 *Model Description*

4.2.1. *Dynamics*

The model used in this study is based on the primitive equations in three-dimensional non-hydrostatic quasi-compressible (Klemp and Wilhelmson, 1978; and Tripoli and Cotton, 1982) form with prognostic equations for u, v, w, p, θ, and the mixing ratios for all hydrometeors (see section 4.2.2 for mixing ratios). The model employs a staggered Arakawa-C grid where dependent variables are specified as

$$\phi(x,y,z,t) = \phi_o(z) + \phi'(x,y,z,t) + \phi''(x,y,z,t) \tag{4.1}$$

in which the base state $\phi_o(z)$ is horizontally homogeneous (as governed by the input sounding) and geostrophically and hydrostatically balanced. $\phi'(x,y,z,t)$ is the perturbation from the base state and $\phi''(x,y,z,t)$ is the sub-grid scale deviation (Straka, 1989). Spacial finite differencing uses a sixth-order version of the minimum aliasing Local Spectral method for momentum (Straka and Anderson, 1992) and a sixth-order flux form of the forward in time Crowley scheme for scalars. Time differencing for u, v, w, and p is done with a leap frog scheme. The model uses outflow lateral boundary conditions (Klemp and Wilhelmson, 1978) and mixing is handled as in Klemp and Wilhelmson (1978). A complete discussion of the dynamics and physics of the model can be found in Straka (1992).

4.2.2 *Microphysics*

The following species of hydrometeors are used in the model: 1) cloud droplets, where q_c represents the mixing ratio of the cloud water to the total hydrometeor content, 2) cloud ice crystals (q_i), 3) rain drops (q_r), 4) snow crystals and aggregates (q_s) and 5) graupel/hail (q_h). All hydrometeors are assumed spherical, with the exception of cloud ice crystals, which are assumed to be hexagonal plates. The bulk production rate of any microphysical hydrometeor (q_x) using a Marshal-Palmer size spectrum is given by

$$\frac{dq_x}{dt} = \left(\frac{1}{\rho_a}\right)\frac{dM_x(D_x)}{dt}N_x(D_x)\ dD_x \tag{4.2}$$

where ρ_a is the density of dry air, M_x is the mass of a spherical hydrometeor having diameter D_x and dD_x is the bin size of the distribution (Straka, 1989). Additional information on the parameterizations of microphysical processes and terminal fall speeds of the hydrometeors is given in Appendix B of Johnson (1992).

4.3. *Initial simulations*

Soundings from 1700 UTC on August 18, 21 and 22 (Figures 3.3, 3.23 and 3.35) were modified using a simple version of a boundary layer model. Using the observed maximum temperature for the day, each sounding's temperature profile was mixed out so that the potential temperature was constant up to the point of intersection with the original temperature profile. The mean wind from the entire depth of the sounding was subtracted out in an effort to keep the simulated storm in the center of the domain. No modifications were made to the moisture profile. Table 4.1 gives calculated quantities and thermodynamic parameters for the modified soundings.

Table 4.1 Sounding characteristics for the three modified soundings.

Date	Time	LI (°C)	CAPE (J kg^{-1})	CCL (m)	LCL (m)	Precip. Water	HTML
8-18-90	1649	-4.3	1723	1694	1897	4.88 cm	3929 m
8-21-90	1658	-3.1	1800	1585	1748	5.05 cm	4633 m
8-22-90	1653	-4.3	1618	1743	1878	3.85 cm	4721 m

Using the modification of the sounding, several simulations were made using the August 22nd sounding. Initial bubble sizes for the simulations were systematically changed until an outflow similar in strength to the largest outflow on the 22nd was achieved. This bubble size was then chosen for all further simulations for comparison purposes.

Each day's simulation was initialized in exactly the same manner using a warm thermal bubble, 6 km wide and 4 km high with a +3 °C perturbation in temperature. The simulations were carried out for 45 minutes in a domain 22 X 22 X 19 km with 600 m resolution in both the horizontal and vertical. Microphysical processes of:

1. sublimation/deposition,
2. melting/freezing,
3. evaporation/condensation and
4. precipitation loading

were examined. Sublimation, melting and evaporation are all cooling or endothermic processes that take heat from the ambient environment. Deposition (gas to ice conversion), freezing and condensation are warming or exothermic processes that give latent heat to the ambient environment. To illustrate, we show a simple version of the vertical equation of motion,

$$\frac{dw}{dt} = g\frac{\theta_v{}'}{\theta} - gl + PGF + \ldots \tag{4.3}$$

The first two terms on the right side of (4.3) can be combined and then differentiating with respect to time to obtain a temperature rate gives

$$\frac{\partial}{\partial t}\left(\frac{dw}{dt}\right) = \frac{g}{\theta}\left(\frac{\partial \theta_v{}'}{\partial t} - \theta\frac{\partial l}{\partial t}\right) + \ldots \tag{4.4}$$

where the right side of (4.4) represents the effect of buoyancy and precipitation loading. The buoyancy term can be approximated for each of the phase changes, sublimation/deposition, freezing/melting and evaporation/condensation by

$$\frac{\partial \theta_v{}'}{\partial t}\bigg|_{phasechange} = \frac{L}{C_p}\frac{\partial l}{\partial t}\bigg|_{phasechange} \tag{4.5}$$

where L is the appropriate latent heat value (fusion, vaporization, etc.) and l is the appropriate mixing ratio (graupel, rainwater, etc.). The precipitation loading term, the second term on the right side of (4.4), also contributes to the vertical acceleration according to the mass of the precipitation particles. The more precipitation particles of a particular type, the greater the contribution to a downdraft from precipitation loading for that type of precipitation.

4.3.1 *General simulated storm characteristics*

We examine the general characteristics of the simulations to identify differences and similarities. Each of the three initial simulations performed produced qualitatively and quantitatively similar storms in terms of the main flow fields (Table 4.2). Each of the simulations had a maximum updraft speed between 25 and 33 ms^{-1} that gave way to a downdraft that varied from 15 to 17 ms^{-1}. These relatively strong downdrafts produced outflows between 30 and 35 ms^{-1}. These outflow speeds are comparable to the maximum observed outflows on the three days of interest (see Tables 2.1, 2.2 and 2.3) and these simulation values should most likely be taken as the potential strength of an outflow on an individual day. It is interesting to note, however, that the maximum outflow strength of the three simulations occurred on the day of weakest observed storms, August 18th.

Table 4.2 Summary of maximum in the flow fields for the three simulations and the related observed maximum outflow ΔV.

Date	Updraft speed	Downdraft speed	Outflow ΔV	Obs. Max. ΔV
8-18-90	29 ms^{-1}	17 ms^{-1}	35 ms^{-1}	30 ms^{-1}
8-21-90	33 ms^{-1}	16 ms^{-1}	30 ms^{-1}	27 ms^{-1}
8-22-90	25 ms^{-1}	15 ms^{-1}	32 ms^{-1}	40 ms^{-1}

Figure 4.1 shows a time series of the maximum updraft speeds below 2 km AGL for all three simulations. The height of 2 km was chosen simply because it was representative of the location just above cloud base during each simulation, and to provide a common point of reference within the storms. Each simulation is generally similar in that each updraft maximum peaks around 800-900 seconds and begins to decrease until 1000-1200 seconds. From this point the maximum updraft speeds increase slightly before tapering off at nearly the same rate.

Figures 4.2-4.4 are vertical cross sections of vertical velocity through the point of maximum rainwater mixing ratio. Panel (a) for each of the figures is at 900 seconds, and it is clear the updraft dominates the vertical velocity field at this time. The August 21st simulated storm is larger at this point than for the other two storms.

By 1200 seconds (Figures 4.2-4.4 panel (b)), each storm has grown significantly larger, and the August 21st storm is still the largest. Each of the storms developed a low-altitude downdraft by virtue of the notch in the upward vertical velocity. The other areas of downdraft on the edges of the storms near the top are compensation motions for the updraft.

Panel (c) of the figures is for 1500 seconds into the simulation and a distinct region of downdraft has formed at low-altitudes at and below cloud base. The downdraft is slightly stronger for the August 21st case but at this point the downdrafts are within a few meters per second of each other.

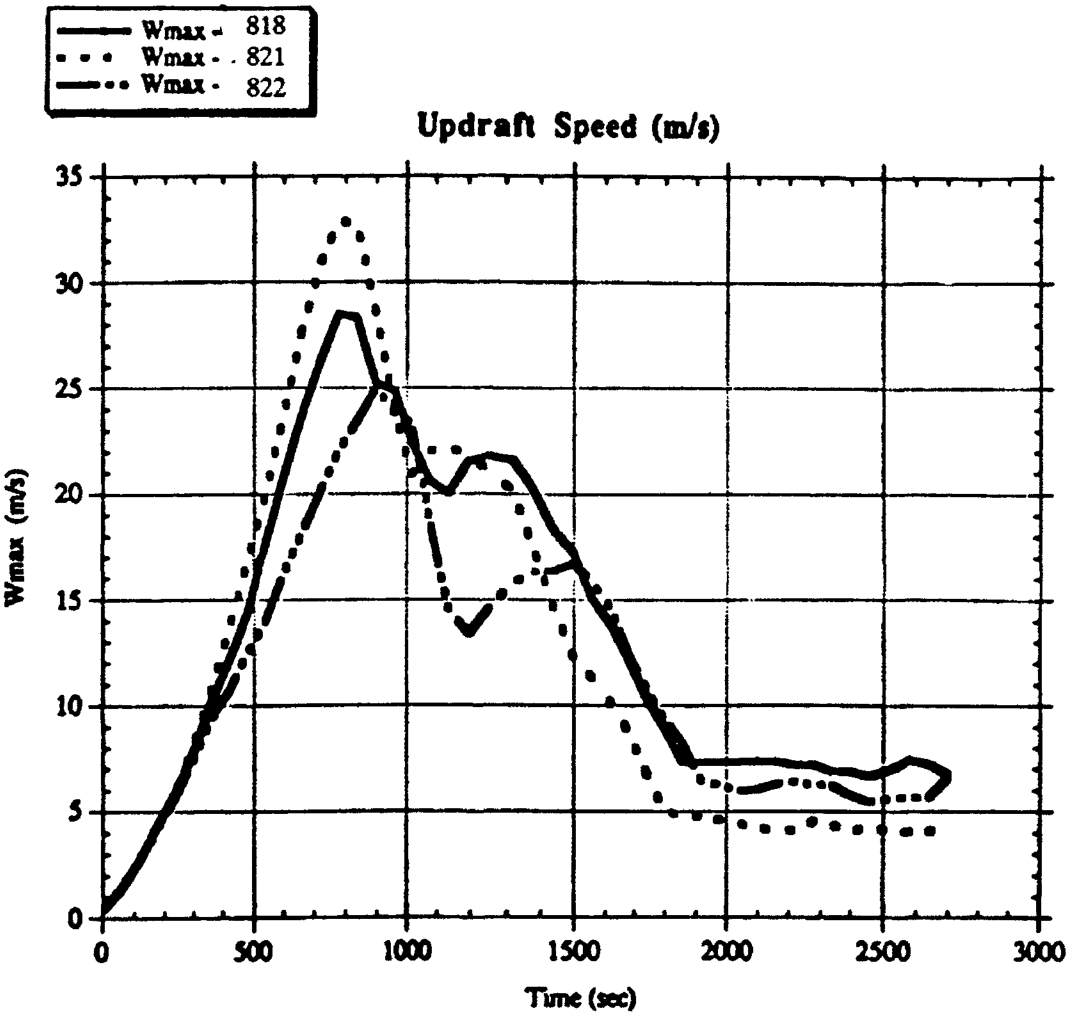

Figure 4.1 Time series of maximum updraft speed for each of the three simulations. The legend at the top left distinguishes the curves.

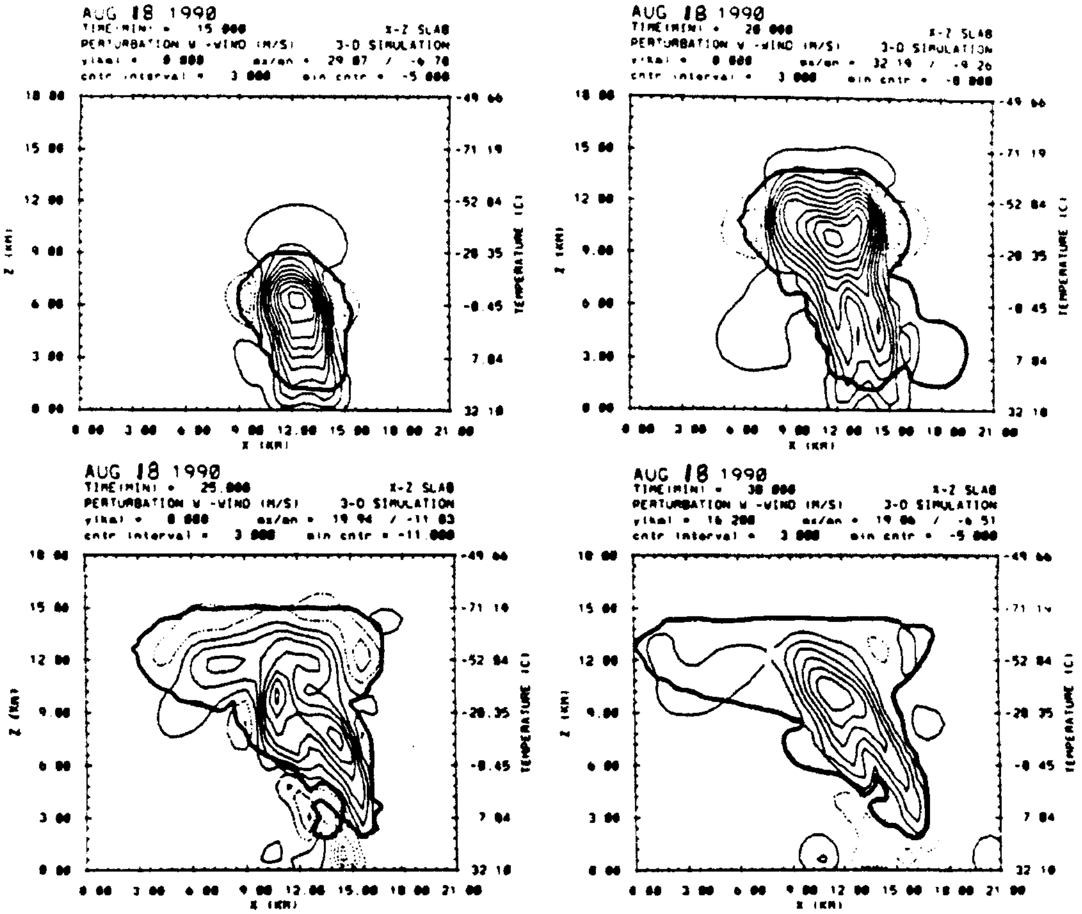

Figure 4.2 Vertical velocity field (perturbation w) and visible cloud for the August 18, 1990 simulation at (a) 900 seconds, (b) 1200 seconds, (c) 1500 seconds and (d) 1800 seconds. The thick line represents the visible cloud. See text for further details.

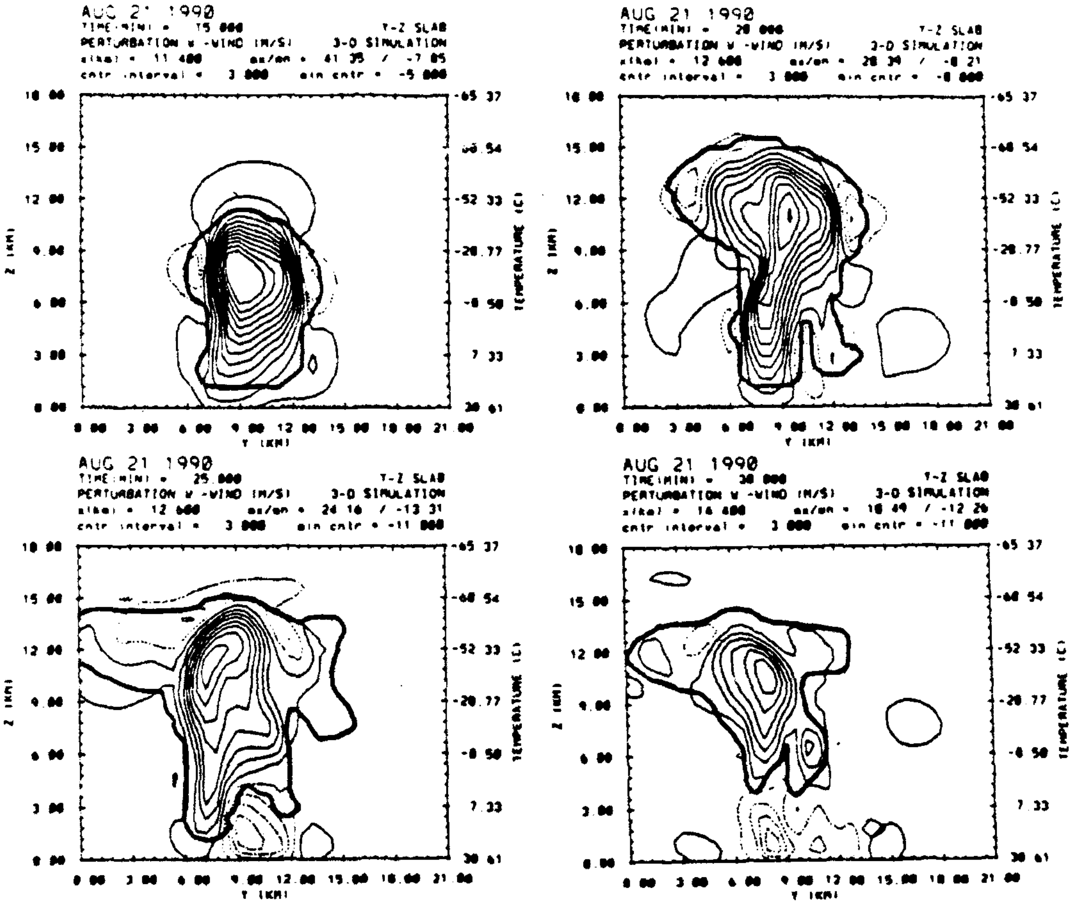

Figure 4.3 As in Figure 4.2, except for August 21, 1990.

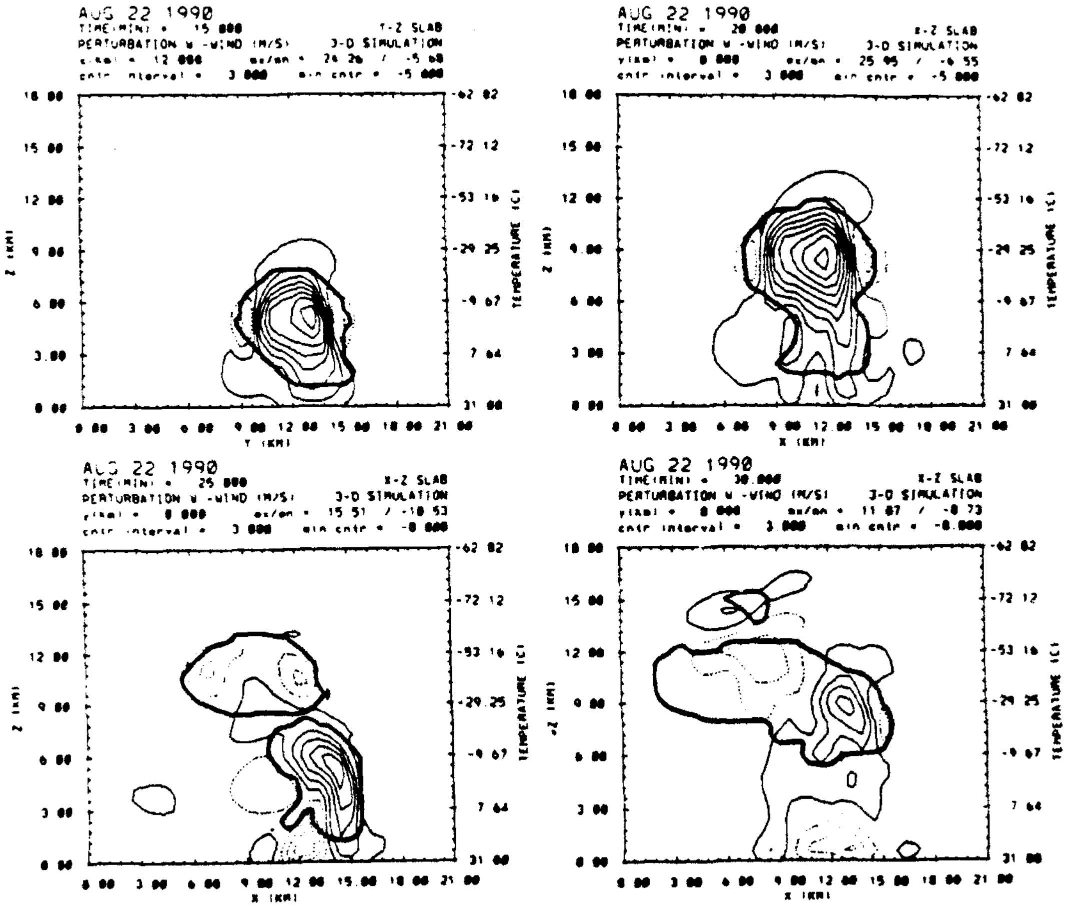

Figure 4.4 As in Figure 4.2, except for August 22, 1990.

By 1800 seconds (Figures 4.2-4.4 panel (d)), the downdraft has widened in all three simulations. The strongest downdraft at this point is also from the August 21st simulation. Figure 4.5 shows the time series of the maximum downdraft speed between 1500 to 1800 seconds. The simulated storm from August 18th produces the largest downdraft speed, even though the August 21st case seemed strongest throughout its lifecycle. However, the difference in the downdraft speeds were not significantly large. Since the vertical cross-sections were taken through the point of maximum rainwater mixing ratio and the maximum downdraft for the August 18th case did not reveal itself, the maximum occurred outside of the main precipitation shaft.

As the downdraft impacts the surface, the outflow begins to accelerate horizontally as pressure gradient forces cause the air to move radially outward from the center of downdraft impact. Figure 4.6 shows the maximum differential velocity at the surface for each of the simulations. Each curve is generally the same, with each peaking around 1800 to 2000 seconds. The largest value is from the August 18th case which also had the strongest downdraft. The moisture profiles in the soundings supported a stronger downdraft for the August 22nd case which in reality was the day with the strongest surface outflows.

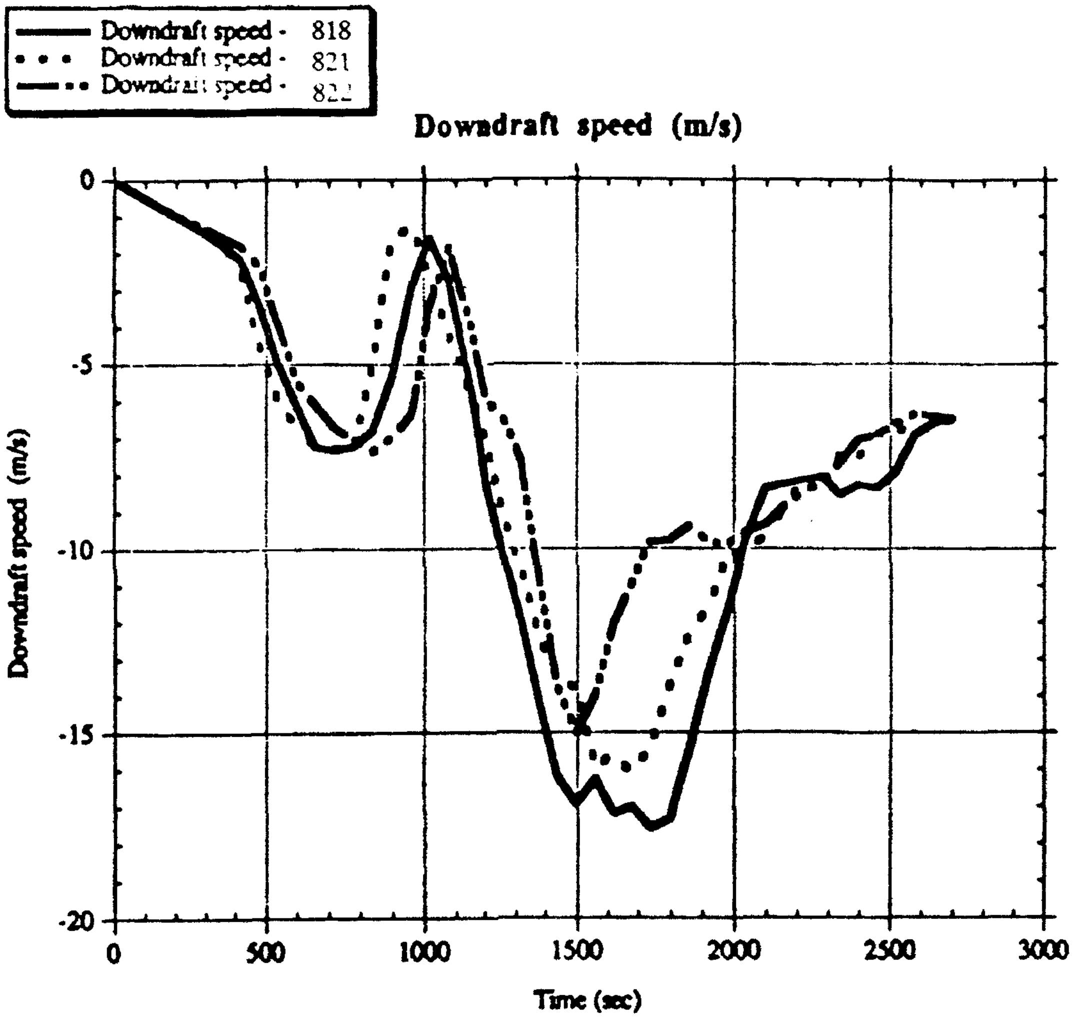

Figure 4.5 Time series of maximum downdraft speed for each of the three simulations. The legend at the top left distinguishes the curves.

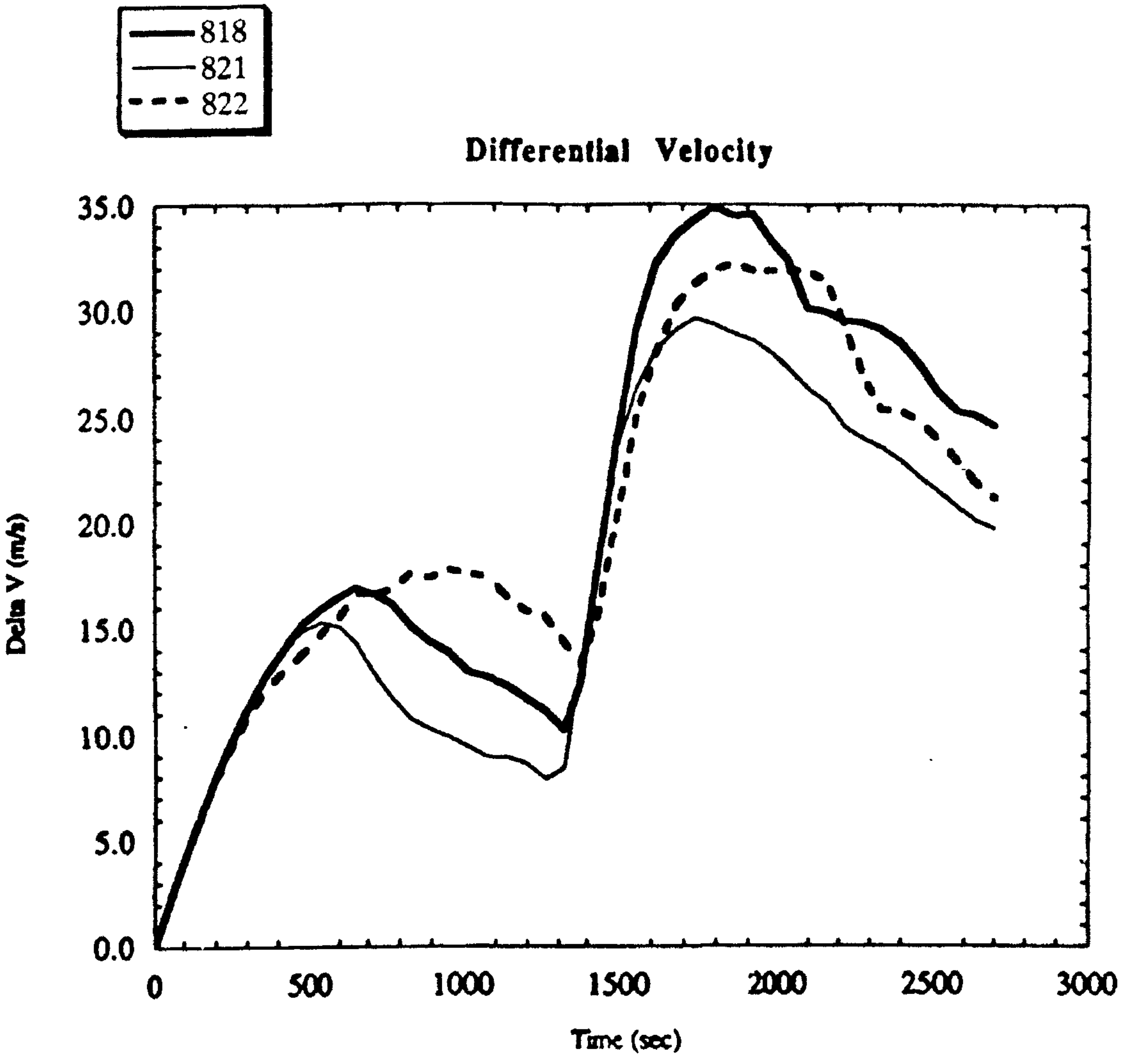

Figure 4.6 Time series of maximum differential velocity for each of the three soundings. The legend at the top left distinguishes the curves.

4.3.2 *Simulations versus observations*

A comparison of the observed storms examined in Chapter III and the simulated storms reveals some discrepancies. The model appears to have over predicted the depth and height of the clouds (compare figures 4.2, 4.3 and 4.4 with 3.5, 3.7, 3.9, 3.13, 3.17 and 3.19). Differences between the modeled and observed storms are most likely due to model sensitivity to initial bubble size, but this is only speculation. We feel that these differences do not adversely affect the results of this study, since the models are used to investigate differences and similarities in outflow characteristics. An accurate estimate of error is not feasible because comparison is being made between radar reflectivities for the observed storms and calculated cloud water in the model. In addition, the scanning strategy used in collecting the radar data is very coarse at the higher elevation angles (see Table 3.1). However, cloud base in the simulations appears to agree with estimates using the CCLs from the soundings. It should be pointed out that cloud base for an updraft is often quite different from the cloud base for a downdraft (see figures 4.2, 4.3 and 4.4) and that the cloud base estimate given by the CCL is that for an updraft. Hence, further references to cloud base are for updrafts.

4.3.3 *Microphysical structure*

Although some differences existed between the soundings and some slight contradictions were noted between the simulations and reality, overall the simulations were generally similar. With this in mind, we now investigate more subtle downburst formation mechanisms by examining the microphysical processes within the simulated storms.

Several microphysical forcing mechanisms were evaluated at 1200 seconds (time of maximum downdraft acceleration) and 1500 seconds (time of peak downdraft speed) for each of the three simulations. These times were chosen in order to identify specific locations within the storm where microphysical forcing mechanisms were contributing to the downdraft.

4.3.3.1 *Deposition/Sublimation*

Figure 4.7 shows the heating rates due to deposition and sublimation at both 1200 and 1500 seconds. At 1200 seconds, each simulation has a maximum in deposition at slightly different heights but the maxima are within 0.02 °C min^{-1} of each other. Deposition of water vapor onto the hailstones or graupel is taking place well above the melting level where only supercooled water drops and ice reside. Each simulation also has a minimum where sublimation is dominant around 5000 m. These minima are also similar in value, varying by only 0.02 °C min^{-1}. Near the melting level, the saturation vapor pressure with respect to ice falls below unity and thus sublimation is possible. The 8-22 case has both the largest maximum in deposition and sublimation. By 1500 seconds, all three simulations show only warming due to deposition with maxima located near 8000 m. The values vary by only 0.01 °C min^{-1} at 1500 seconds. The value for heating rate due to deposition and submlimation are very small and could possibly be neglected

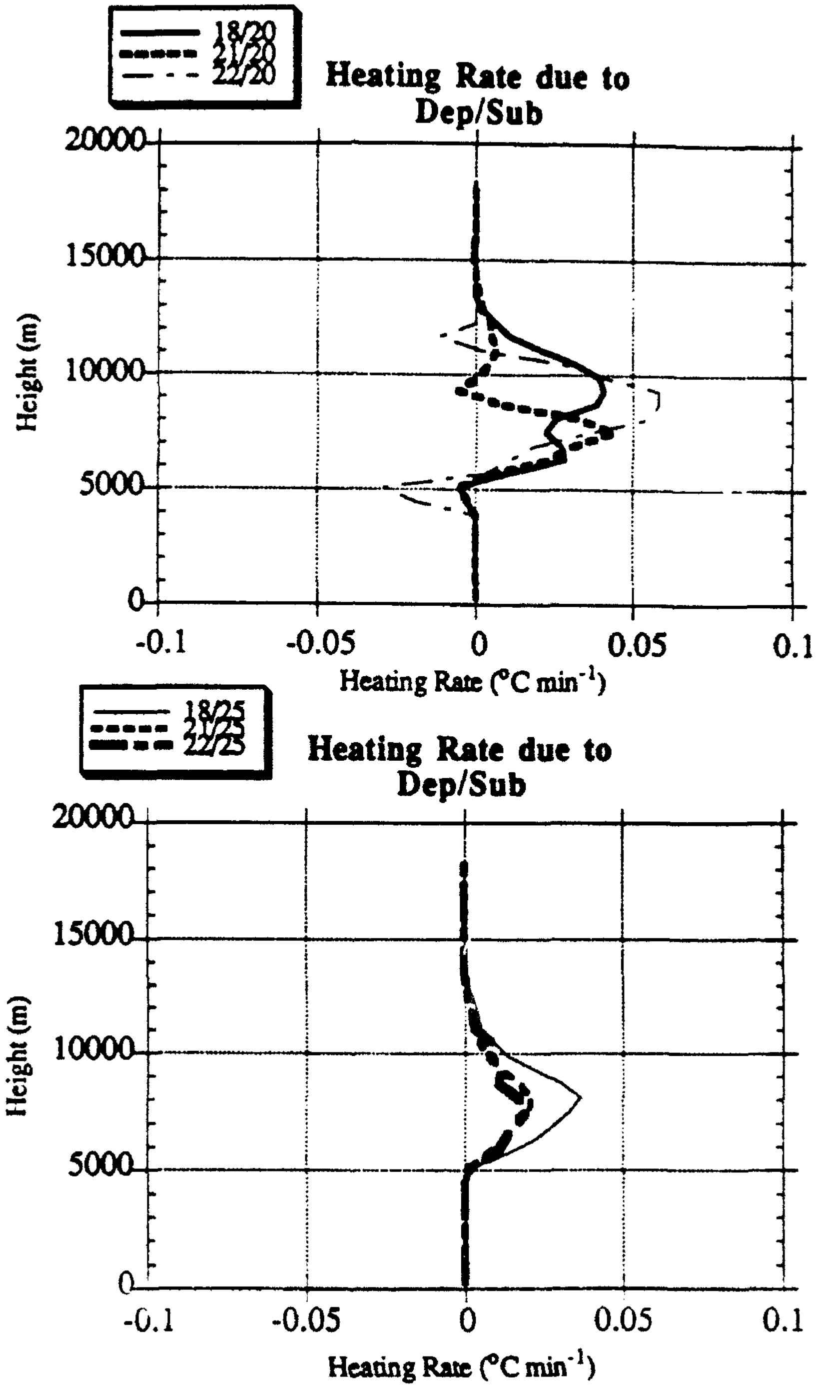

Figure 4.7 Vertical profiles of the contributions to the heating rate by deposition and sublimation for the three initial simulations at 1200 and 1500 seconds. Legend at the upper left distinguishes the curves. See text for details.

as will be seen in the following discussion.

4.3.3.2 *Freezing/Melting*

Figure 4.8 shows the heating rates due to freezing and melting at both 1200 and 1500 seconds. The first note of importance is that the values for freezing and melting are an order of magnitude larger than those for deposition and sublimation. At 1200 seconds, each simulation is characterized by a peak in warming, where freezing dominates around 5500 m, and a peak in cooling, where melting dominates near 4000 m (at the melting level). Temperatures from the soundings near 5500 m are generally around -4.0 °C and hail and graupel are abundant due to growth at these temperatures. A review of the rainwater field (not shown) reveals that precipitation is only beginning to reach the surface at 1200 seconds. The 8-18 simulation has a slightly higher value in the warming peak but the cooling value is the same as the other two simulations.

By 1500 seconds the peak in warming remained but had decreased in magnitude. The peak in cooling had moved down slightly, increased in value and occurred over a larger depth. This increase can be seen in Figure 4.9, where the total amount of ice and liquid increases significantly from 1200 to 1500 seconds. At 1500 seconds, the rainwater field reveals that precipitation is most definitely reaching the surface. Thus, the majority of the graupel/hail has fallen out and began to melt by 1500 seconds, decreasing the freezing impact and increasing the melting impact on the cooling rate.

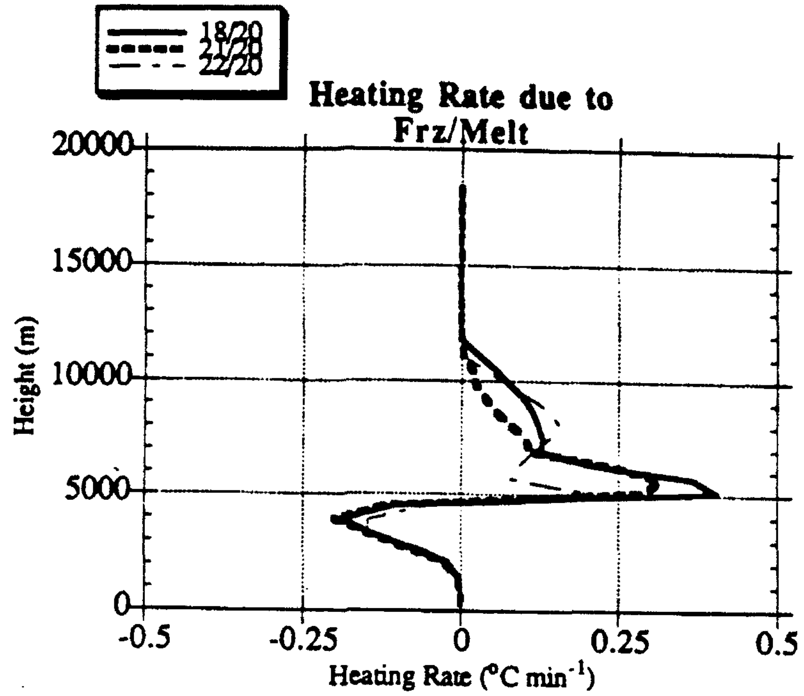

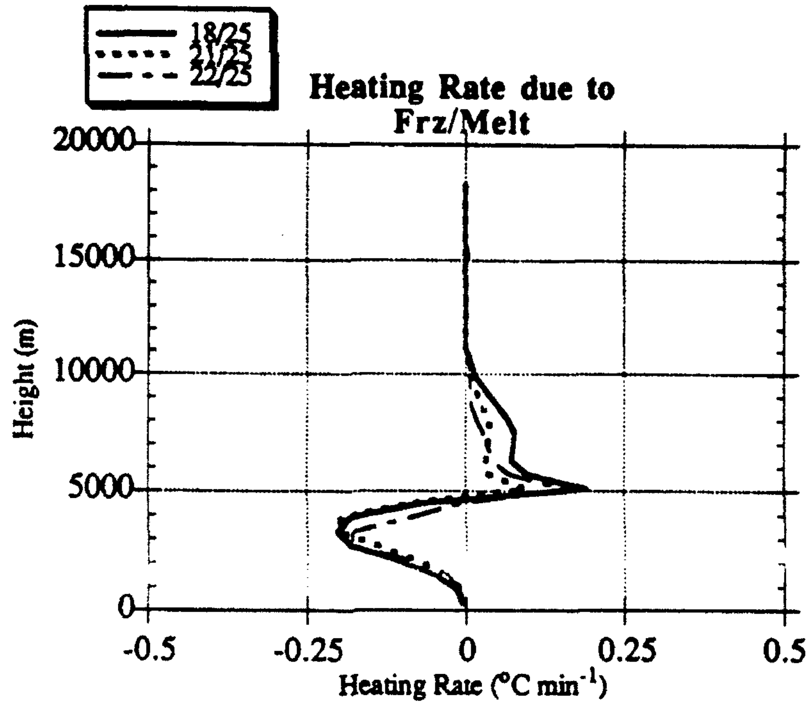

Figure 4.8 As in Figure 4.7, except for freezing and melting.

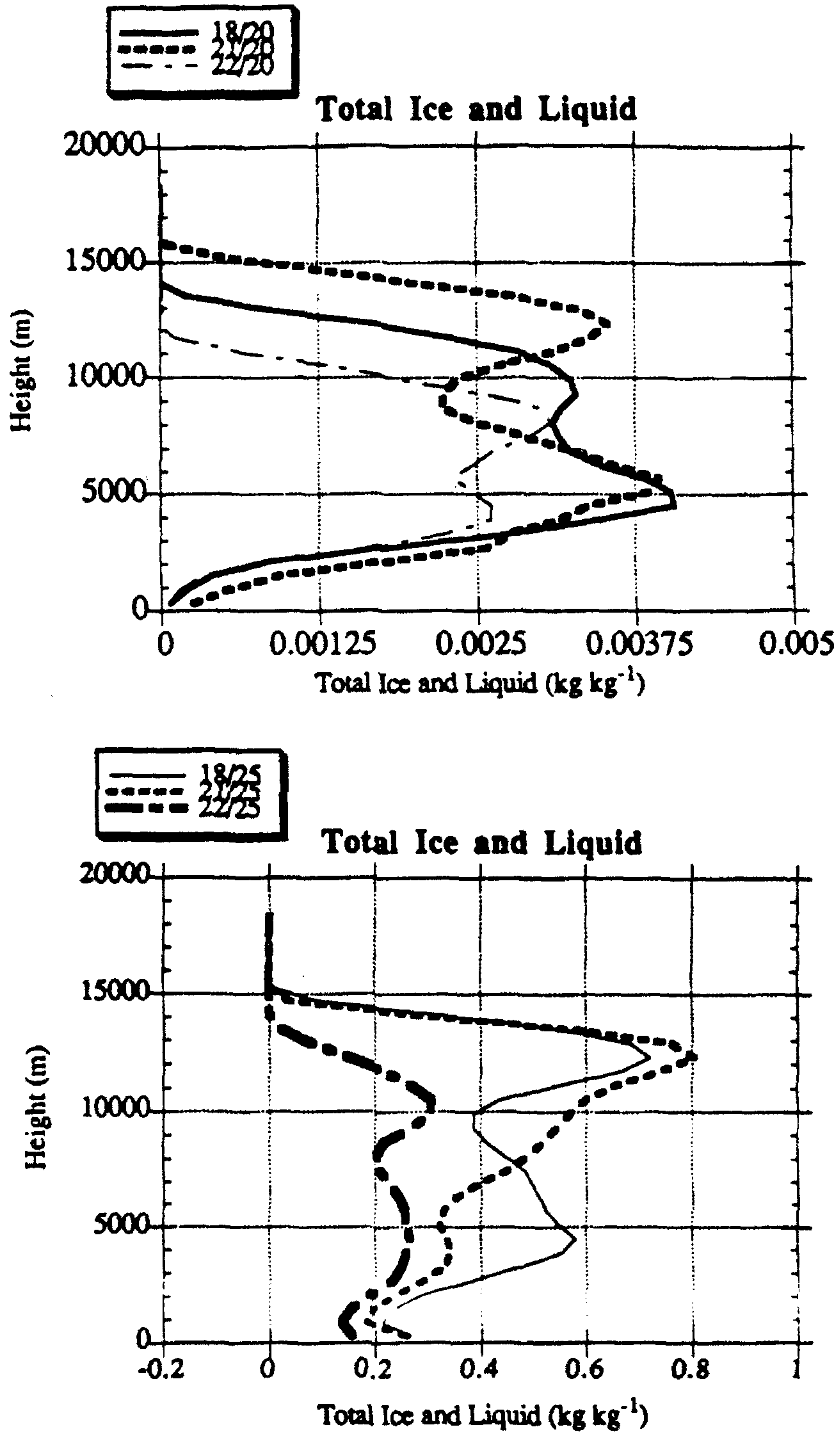

Figure 4.9 Total (ice and liquid) mixing ratio of precipitation within the three simulated storms at 1200 and 1500 seconds. Legend at the upper left distinguishes the curves.

4.3.3.3 *Condensation/Evaporation*

Figure 4.10 shows the heating rates due to condensation and evaporation for both 1200 and 1500 seconds. By 1200 seconds, the condensation effect is very small: thus, evaporation dominates. At 1200 seconds, all three simulations have a peak in cooling due to evaporation around 1000 m, as at this time precipitation is beginning to fall into the low-altitudes. Evaporation is occurring throughout the depth below 4000 m but is strongest below 2000 m (cloud base for the three simulations ranges from 1600 to 1750 m) and peaks at a value between -0.09 °C min^{-1} and -0.15 °C min^{-1}.

By 1500 seconds, cooling due to evaporation has significantly increased with the maximum occurring at the surface as precipitation is well underway and peak values of cooling ranging from -0.52 °C min^{-1} to -0.63 °C min^{-1}. More precipitation (in this case, liquid precipitation) allows for more evaporational cooling.

4.3.3.4 *Total heating rate*

Figure 4.11 shows the total heating rate due to deposition, sublimation, freezing, melting, condensation and evaporation. At 1200 seconds, the region above the melting level is undergoing a net warming that is dominated by freezing. Comparison of Figures 4.8 and 4.11 above the melting level reveals nearly identical profiles at 1200 seconds. Below the melting level, the total heating rate is a net cooling effect that is dominated by evaporation below cloud base (below 1750 m). Thus, at 1200 seconds, the time of maximum acceleration of the downdraft, melting and evaporation are dominant in

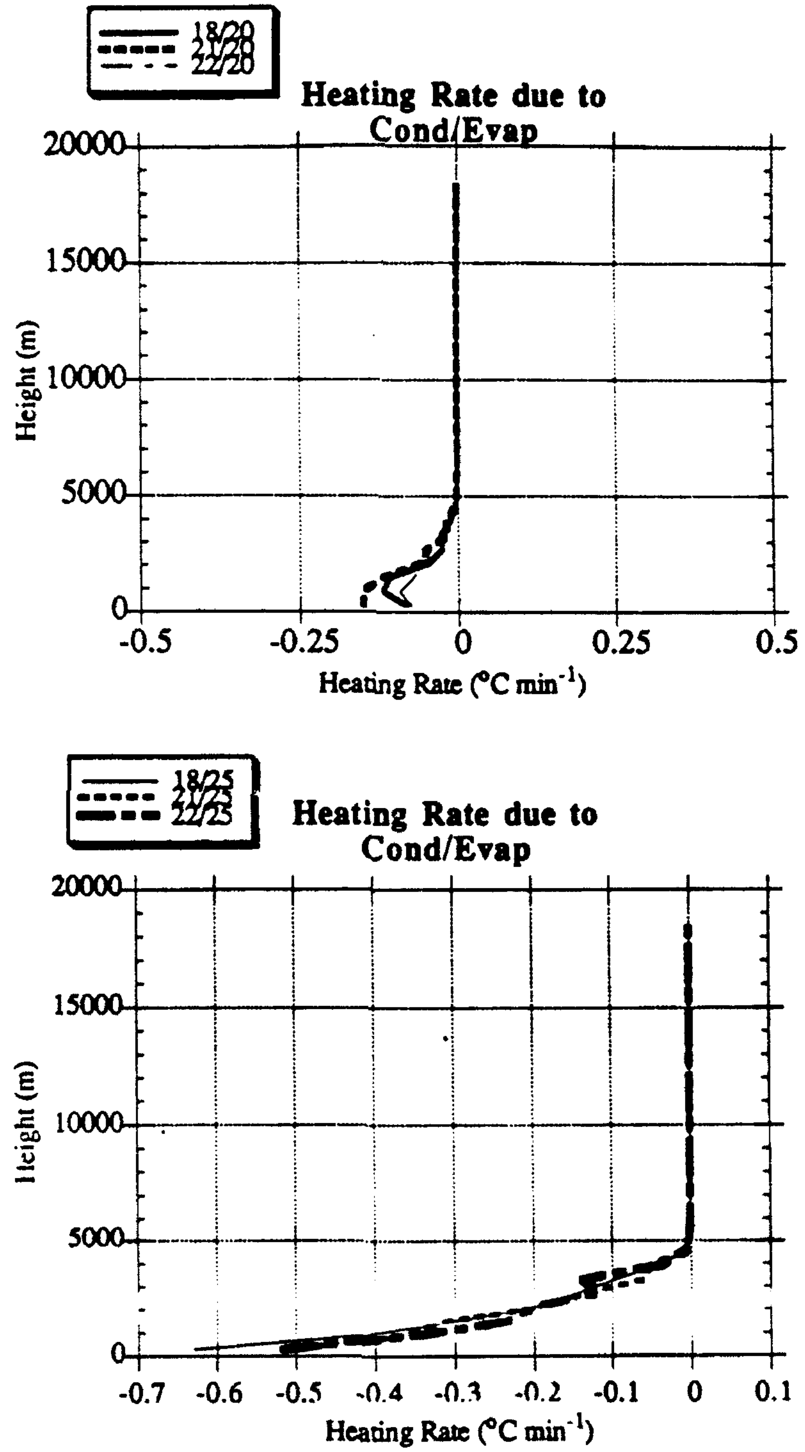

Figure 4.10 As in Figure 4.7, except for condensation and evaporation.

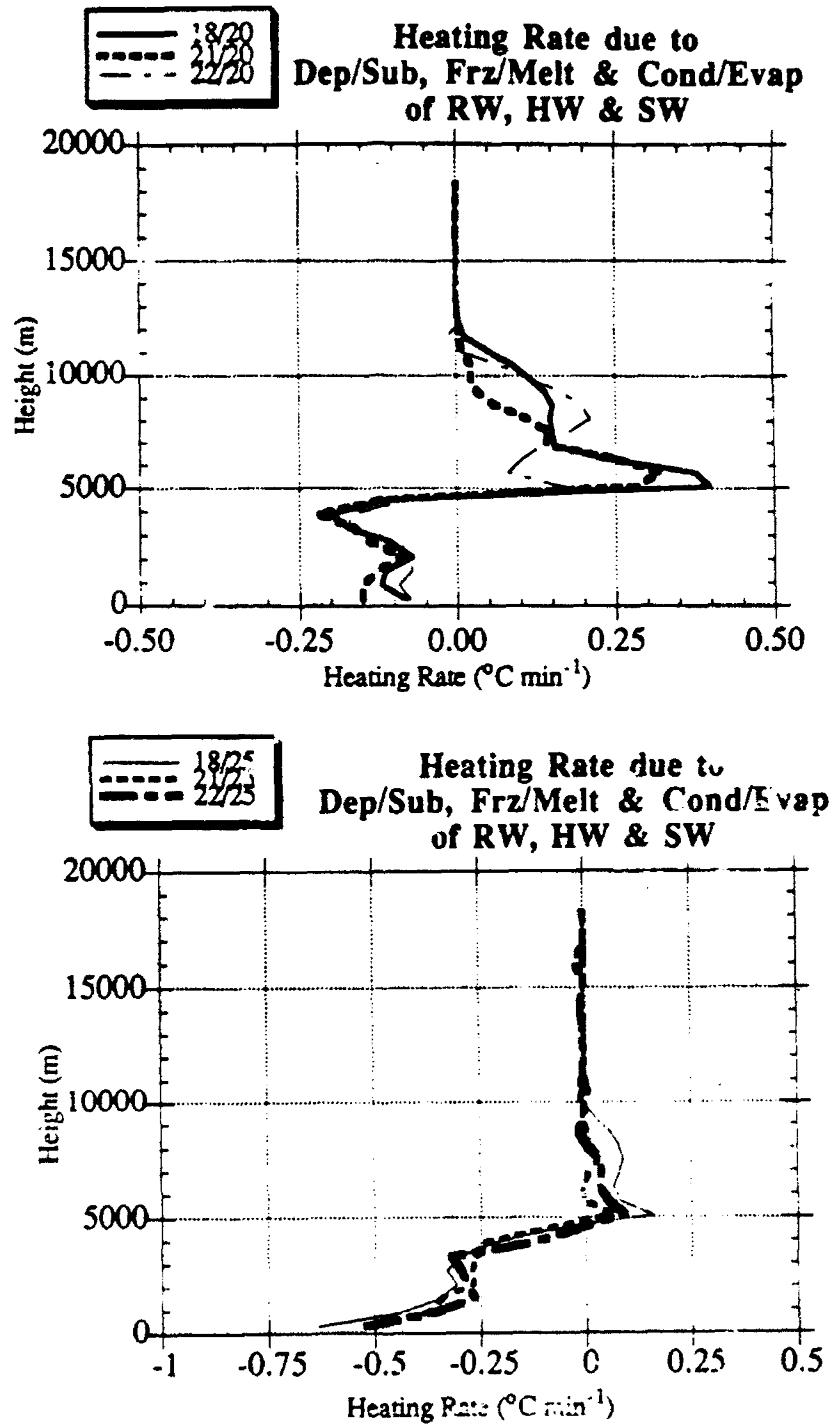

Figure 4.11 As in Figure 4.7, except for the total temperature rate.

producing negative buoyancy.

By 1500 seconds, the net warming above the melting level is tremendously smaller than at 1200 seconds, but continues to be dominated by freezing. At this time of peak downdraft, melting directly below the 0 °C level and evaporation below cloud base have both increased but the entire layer below the melting level is dominated overall by evaporational cooling. Evaporational cooling below cloud base is the dominant thermodynamic forcing for these downdrafts; cooling by melting is secondary as some hail does fall below cloud base but melts before reaching the surface.

4.3.3.5 *Precipitation loading*

Figure 4.12 shows the precipitation loading effect for both 1200 seconds and 1500 seconds. Precipitation loading is given by gl where g is the acceleration due to gravity and l is the mixing ratio of the total amount of precipitation particles. At 1200 seconds acceleration due to precipitation loading exhibits two peaks, one above 8000 m (ice only) and another at 5000 m. This lower peak is located where ice and liquid co-exist, near the melting level. There is little, to no, effect by precipitation loading in the lowest 2000 m at 1200 seconds. By 1500 seconds, the two peaks mentioned above remain but the effect of precipitation loading now extends to the surface as precipitation reaches the ground.

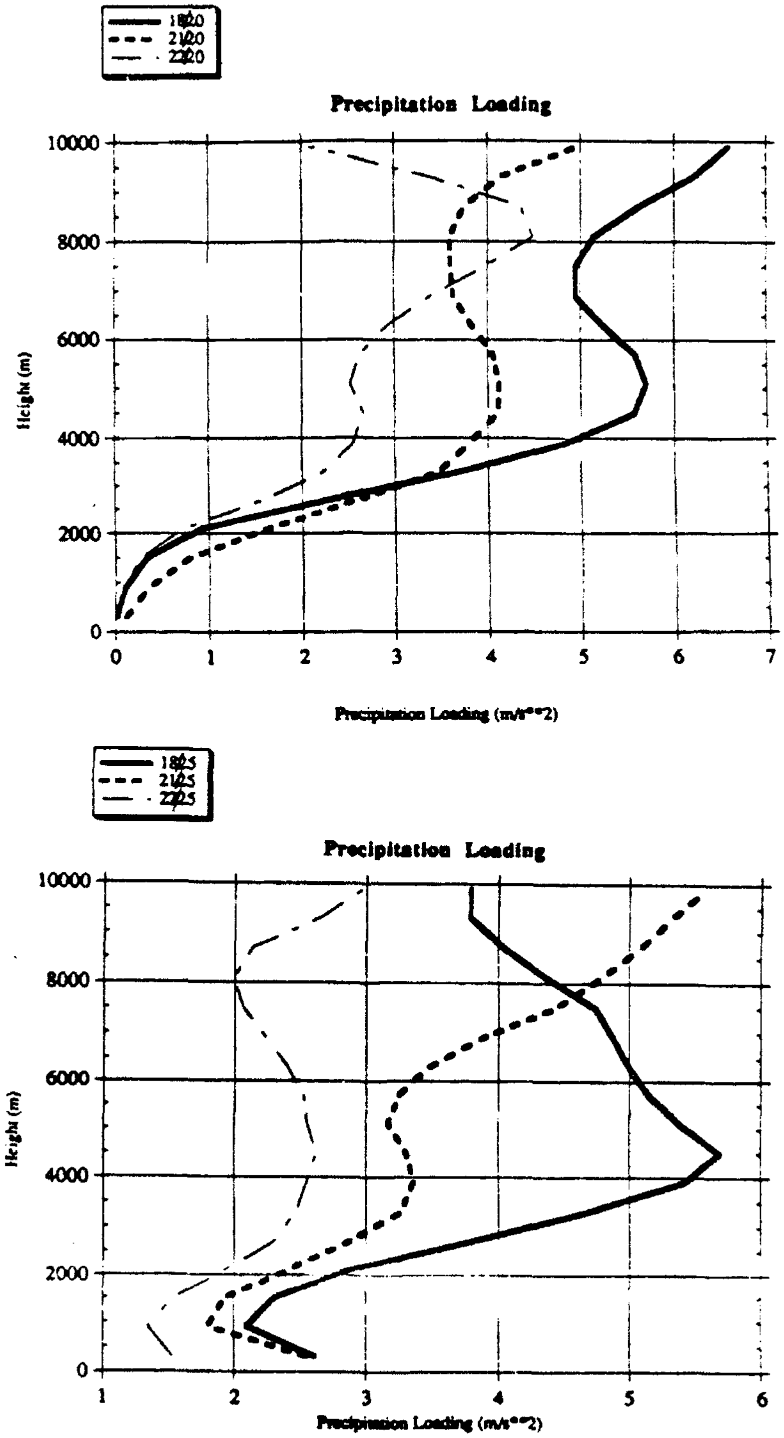

Figure 4.12 Precipitation loading for the three simulations at 1200 and 1500 seconds. Legend at the upper left distinguishes the curves.

4.3.3.6 *Summary and discussion of microphysics*

The individual components of the heating rate for the three simulations were remarkably similar given that the environments have minor but detectable variations (Table 4.3). Deposition and sublimation are an order of magnitude smaller than the other two components of the heating rate. Melting dominates the cooling process near and below the 0 °C level to near cloud-base. Below cloud-base, melting continues but evaporation is the dominant contributor to negative buoyancy. Precipitation loading contributed to the net downward motion but not as significantly as melting or evaporation. The location and relative importance of the microphysical processes are in agreement with Chen (1986), Proctor (1988) and Knupp (1989). The dominance of melting and evaporation when compared to loading is also in agreement with Srivastava (1985).

The identification of three regions of microphysical processes is not unexpected. Chen (1986) and Knupp (1989) found these same regions. Above the melting level, sublimation, although quite small, dominates. Between the 0 °C level and cloud-base, melting dominates and below cloud-base, evaporation dominates. Precipitation loading is of course strongest at the precipitation center. The low-altitude (below cloud-base) precipitation loading equivalent cooling rates for the three simulations varied from 0.008 °C min^{-1} for the 8-18 case to 0.136 °C min^{-1} for the 8-21 case at 1500 seconds. These values are smaller than the values obtained by Chen (1986) in his 2-D 'wet' downburst simulation. The strongest precipitation loading effect is at cloud-base where evaporation of liquid precipitation is only minor, but its coupling with melting and evaporational

Table 4.3 Summary of cooling rates due to microphysical processes for three initial simulations. Values in parentheses are the heights AGL where the maximum in the process occurred.

Date	Sub (°C min^{-1})	Melt (°C min^{-1})	Evap (°C min^{-1})	Prec. Load. (°C min^{-1})
8-18-90	0.01 (5000 m)	0.2 (4000 m)	0.62 (sfc)	0.008 (4900 m)
8-21-90	0.01 (5000 m)	0.2 (4000 m)	0.52 (sfc)	0.136 (5000 m)
8-22-90	0.02 (5000 m)	0.18 (3000 m)	0.52 (sfc)	0.017 (4900 m)

cooling make the region below cloud base more significant for these simulations.

Cooling rates due to melting are a maximum at, and just below, the melting level at 1500 seconds. All three simulations have a maximum cooling rate due to melting around 0.2 °C min^{-1}. This value is significantly smaller than the maximum values of Chen's simulation.

The evaporational cooling for our simulations reach a maximum of 0.5 °C min^{-1} - 0.6 °C min^{-1} at the surface at 1500 seconds. Again, Chen's value for evaporational cooling rate was higher at 2.4 °C min^{-1}. The differences in the magnitude for the cooling rates are most likely due to the much larger storm produced in Chen's simulation that produced a ΔV of 42 ms^{-1}. It is also important to note that evaporative cooling does not reach a maximum until after the outflow maximum has occurred even though it dominates prior to maximum outflow.

Examination of the detailed microphysics of the three simulations did not reveal any significant differences that could possibly explain the observed differences in outflow strength from the observational study. Even though the environments for the three days appear very similar, different strengths of outflows were observed. The numerical simulations on these three days confirm that the environments were quite similar since the microphysical structures were similar (only the precipitation loading showed any significant difference) and the resulting outflow fields were also similar. Thus, a reason for the observed variability, other than the kinematic differences of the observed storms and differences in microphysical structure, needs to be determined. In the observations, it was noted, that cool outflows did propagate underneath pre-existing storms and then the downdraft from these new storms fell "into" the old outflow. Proctor (1988), Wolfson (1990) and Droegemeier (1992) have verified that a surface-based stable layer can decrease the resulting outflow of a storm by dispersing the energy of the downdraft in the form of gravity waves along the top of the stable layer. However, the simulations that verified this phenomenon were performed by inserting a stable layer after the storm was well underway. It is possible that a surface-based stable layer could exist in a particular area from previous convection and not have been tracked by the radar due to lack of a reflectivity thin line or weak winds. Could a storm develop above that stable layer and then produce an outflow on "top" of that stable layer?

4.4 *Stable layer simulations*

To address this question, the August 18th modified sounding was changed further and two additional simulations performed to assess the effect of a surface-based stable layer on the strength of surface outflows. A 600 m layer of cool (3 °C and 6°C constant with height negative temperature perturbation layers) air was inserted into the domain and then the 8-18 simulation was performed as before. One would expect the updrafts for these two simulations to be somewhat weaker than before, with perhaps similar downdrafts provided the maximum downward velocity occurs above the stable layer. Figure 4.13 shows the updrafts speeds for the original 8-18 simulation and the two stable layer simulations. The updrafts evolve more slowly with the presence of the stable layer, and lag by about 100 seconds. The updrafts for the stable layer cases are weaker but not significantly indicating that the majority of the updraft air is not being drawn from the lowest 600 m of the domain. Thus it appears highly possible that a storm could form above a surface-based stable layer and grow to a significant size and produce an outflow of its own.

Figure 4.14 shows a comparison of the downdrafts for the original 8-18 simulation and the two stable layer simulations. The maximum downdraft did decrease by about 2 ms^{-1} for the stable layer simulations, but this is most likely due to weaker updrafts. The evolution of the downdrafts remains consistent for all three simulations.

With the updrafts and downdrafts having been only slightly affected by the presence of the stable layers, what effect will the stable layers have on the resulting outflows? Figure 4.15 shows the resulting ΔV's for the three simulations. The outflow strength in the 3 °C simulation is 26 ms^{-1} which is considerably less than the 35 ms^{-1} for

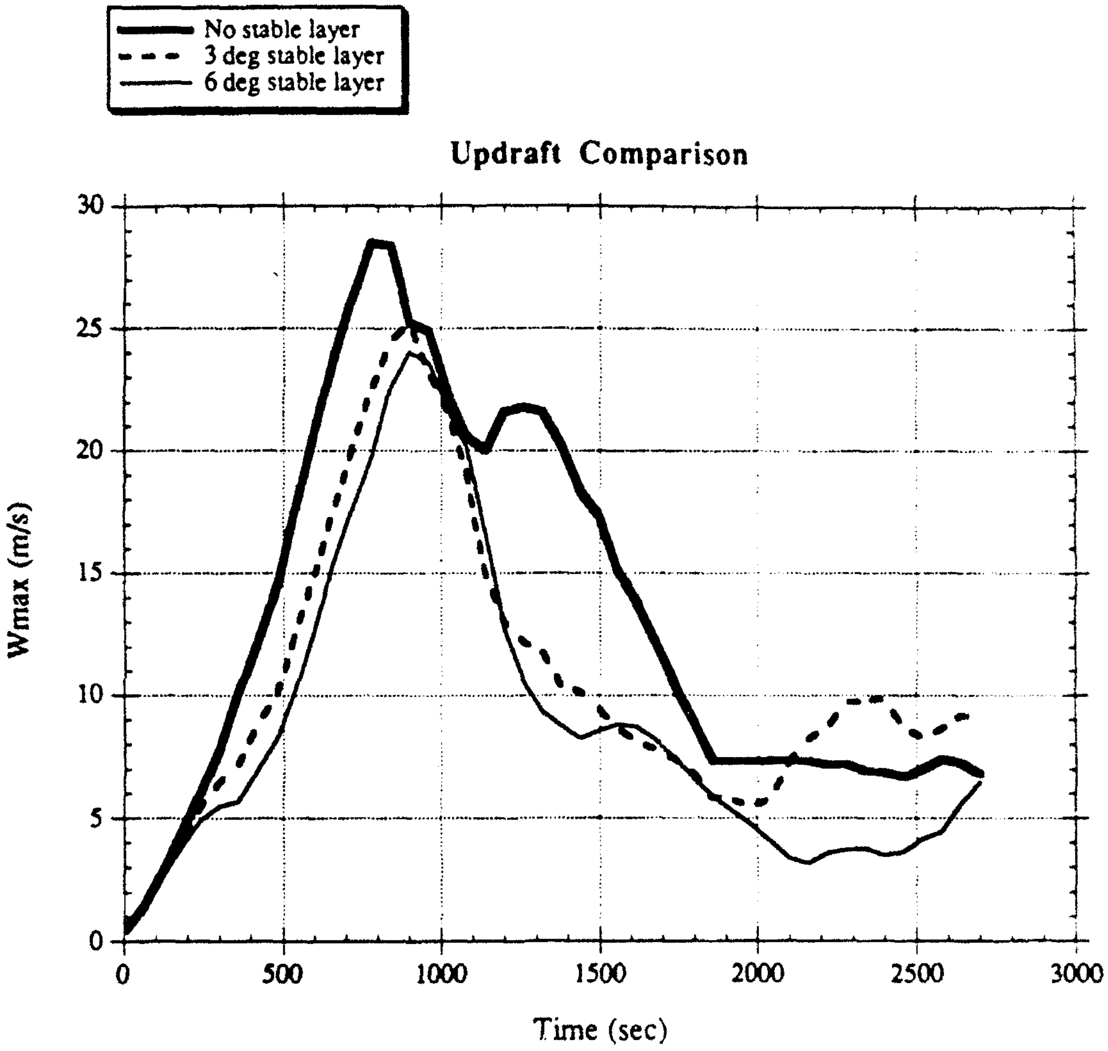

Figure 4.13 Comparison of updrafts from the 8-18 sounding simulations using the original sounding, a 3 °C stable layer at the surface, and a 6 °C stable layer at the surface. Legend at upper left distinguishes simulations.

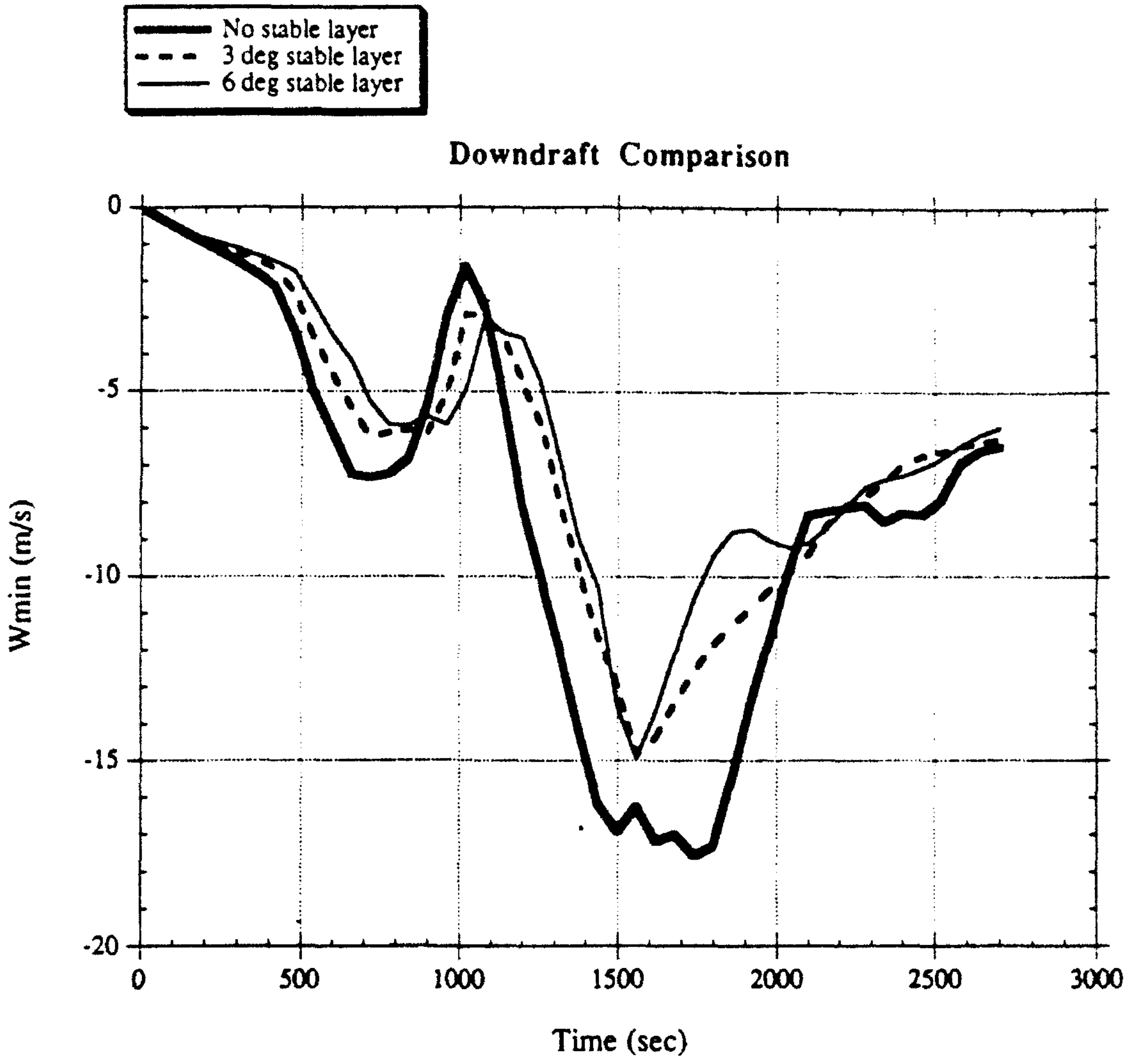

Figure 4.14 As in Figure 4.13, except for downdrafts.

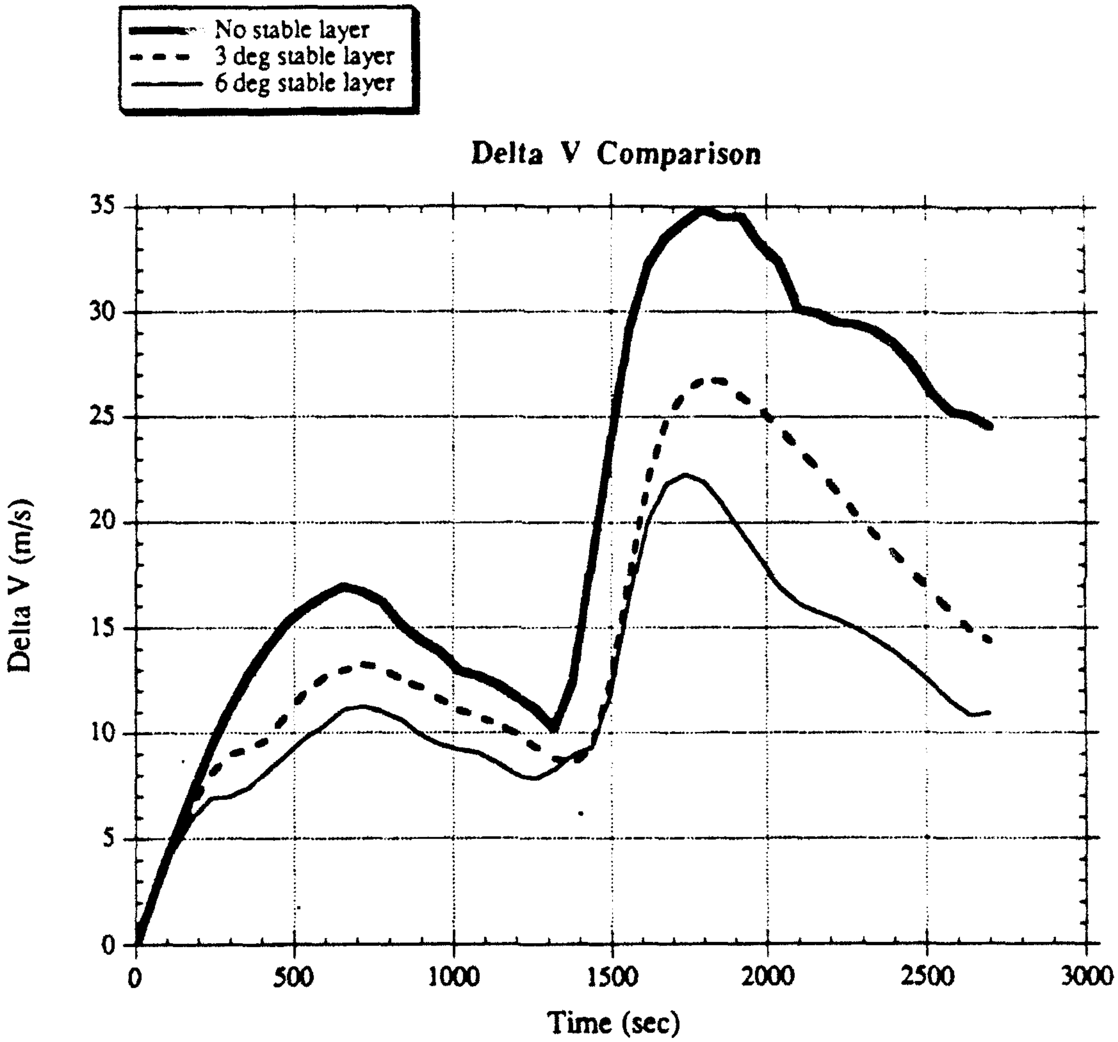

Figure 4.15 As in Figure 4.13, except for outflow ΔV's.

the original simulation. The 6 °C simulation produced an even weaker ΔV of 22 ms^{-1}.

Having eliminated differences in the kinematics of the observed storms and variations in the microphysical forcing mechanisms, *the outflow strength variation appears to be at least partly explained by the presence of surface-based stable layers.* This raises an interesting problem for predicting outflow strengths with Doppler radar algorithms. If an algorithm uses only kinematic and reflectivity precursors within a storm, an undetected stable layer could cause the prediction to be too high and potentially raise the false alarm rate of the algorithm.

To further address the effect of a stable layer on storm evolution, a series of additional model simulations were performed. Using the same initial conditions as in all previous simulations, we ran 14 additional simulations. In this manner we were able to evaluate the sensitivity of the outflow speeds to the depth and strength of the stable layers. We suspected that, at some depth and strength, no storm would be produced in the simulation and that the effect on the outflow strength would monotonically decrease with increasing strength and depth. Table 4.4 gives the results of these model simulations in the form of updraft, downdraft and outflow speed.

Examination of the updraft speeds reveals that the control run (no-stable layer) had a 28.5 ms^{-1} updraft and the updraft speeds are within 85% of the control run for both the 0.6 and 0.9 km stable layers at all stable layer strengths. Increasing the depth of the layer to 1.2 km or more for all stable layer strengths drastically decreases the updraft speeds. The updraft results all look fairly reasonable, with the exception of the 6 °C - 1.8 km

Table 4.4 Model results from sensitivity simulations in the form of (top) updraft maximum, (middle) downdraft maximum and (bottom) outflow maximum.

Updraft Speed (ms^{-1})						
ΔH/ΔT	0 km	0.6 km	0.9 km	1.2 km	1.5 km	1.8 km
0 °C	28.5	*	*	*	*	*
2 °C	*	26.3	26.4	21.6	21.9	23.2
4 °C	*	25.2	25.3	17.9	16.5	18.0
6 °C	*	24.0	24.2	6.5	7.7	15.8

Downdraft Speed (ms^{-1})						
ΔH/ΔT	0 km	0.6 km	0.9 km	1.2 km	1.5 km	1.8 km
0 °C	17.6	*	*	*	*	*
2 °C	*	16.1	16.2	17.6	17.6	16.3
4 °C	*	14.0	14.1	8.3	9.7	10.2
6 °C	*	14.9	15.1	3.7	3.8	6.4

Outflow speed (ms^{-1})						
ΔH/ΔT	0 km	0.6 km	0.9 km	1.2 km	1.5 km	1.8 km
0 °C	17.7	*	*	*	*	*
2 °C	*	15.9	15.9	12.4	12.4	14.8
4 °C	*	12.6	12.4	3.7	8.7	13.1
6 °C	*	11.9	12.2	4.1	4.3	10.1

deep scenario. We would have expected the updraft for this case to be somewhat similar to that of the 6°C - 1.5 km deep scenario. However, the updraft speed doubles for the deeper of these two scenarios. This spurious result is not fully understood, but the fact that a portion of the "initial bubble" was located within the stable layer is know to cause such spurious results.

The downdrafts and outflows have a trend similar to that of the updrafts. Generally, the stronger the updraft, the stronger the downdraft and outflow. Weak downdrafts and outflow occur if the strength of the stable layer is at least 4 °C and the depth is at least 1.2 km for this Florida environment.

It is the type of information contained in Table 4.4 that can be used in an expert system-type algorithm for predicting the strength of an impending downburst. However, it must be recognized that these model results are at most valid for a Florida summertime environment. Thus, similar sensitivity tests would need to be performed for other environments.

CHAPTER V

SUMMARY AND DISCUSSION

5.1 *Summary*

The observed variability of outflow strength in Florida downburst-producing storms has been documented. In particular, storms from three days in August, 1990 exhibited variability both among the days and within the same day. The variability took place among similar storms in similar environments. A process of elimination of possible reasons for the variability, or possible indicators of the variability, was undertaken in an attempt to uncover an explanation. The investigation included examination of downburst precursors, as observed by Doppler radar to determine if the precursors were indicators of the variability. Differences among the individual cases were noted both in the type and strength of velocity precursor. Similarities were noted in the trend of the slantwise

VIL for each of the storms and the reflectivity field did reveal descending cores for each of the 8 cases. The slantwise VIL tended to peak and began to decrease prior to any significant increase in the surface outflow. Storm mass also showed some indication of relative strength of the outflows. However, none of the similarities or differences in either the reflectivity or velocity fields indicated that variability in the outflow strengths should occur.

Expecting more subtle mechanisms, we examined detailed microphysical processes from 3 numerically simulated storms that had the soundings from the three days of observations as initial conditions. Three important regions associated with the production of the downbursts were identified. Above the melting level, the principle cooling process is sublimation. But, sublimation is at least an order of magnitude less important than other processes in producing negative buoyancy throughout the depth of the storm. Between the melting level and cloud-base, the dominant cooling process is melting of hail/graupel. Below cloud-base, melting is important but evaporational cooling dominates. Precipitation loading was also examined and was determined of minimal importance in producing downward acceleration. Overall, the analysis of the microphysics did not reveal any clear ties between microphysical variations and the intensity of the outflows. After eliminating the above mechanisms, we reasoned that the observed variability could perhaps be explained by very shallow surface-based stable layers whose principle effect would be to diminish the outflow strength through dispersion of energy by gravity waves. Two simulations (3 °C and 6 °C negative potential temperature perturbation 600 m deep layers) were performed with a stable layer at the surface in the domain and the clouds were allowed to grow above this layer.

The updraft and downdraft speeds were only slightly decreased for the stable layer simulations as compared to the original non-stable layer simulation. Thus, it appears that the majority of the updraft air is being drawn from above the stable-layer. The outflow ΔV for the stable layer simulations was decreased by 8 ms^{-1} for the 3 °C run and 13 ms^{-1} for the 6 °C run. The outflow decrease is in agreement with studies by Proctor (1988), Wolfson (1990) and Droegemeier (1992). However, this is the first study to insert the stable-layer into the domain at the beginning of the simulations and we still attained virtually the same storm as was produced with no stable layer but, with different resulting outflow.

Additional model simulations were performed to examine the sensitivity of the outflow speeds to the strength and the depth of the surface-based stable layers. It was found that at some stable layer strength and depth no storm was produced during the simulation and that below that point, the speed of the outflow generally decreased with increasing strength of stable layer for each depth. The outflow speeds were generally not effected more by one particular depth of a stable layer for the 2 °C scenario. Stronger stable layers did have a more decreasing effect on the outflow speeds up to the point of no storm development.

5.2 *Discussion*

The result of a simulated storm over a surface-based stable layer being nearly identical to a simulated storm without the stable layer introduces a problem into the prediction of downburst strengths. The use of downburst precursors to predict the strength of an impending downburst is still under debate; however, some success has been shown (Campbell and Isaminger, 1990). If a shallow stable layer exists beneath a downburst producing storm, the event most certainly may still be a hazard to aviation (Wolfson, 1990) but the prediction of the outflow strength as seen by a Doppler radar may be too high and create poor results for an algorithm.

The cases in this study involved trackable cool outflows that moved underneath other storms. It appears that in a Florida environment, the outflows will be trackable for the most part via reflectivity thin lines and windshifts. Once a cool outflow has moved underneath a storm, then the problem becomes the determination of the strength of the stable layer. As seen in this study, a difference of only 3 °C can make a 20% difference in the strength of the surface outflow. Of course, having surface sensors in the vicinity of a storm would be a tremendous help as with the mesonet in this study; however, it is certainly out of the question to expect such a large number of surface sensors. In the terminal environment LLWAS sensors will be in place, but these sensors only take wind measurements. A more promising method of measuring the strength of stable layers is the combined use of aircraft temperature measurements from the Aeronautical Radio Inc. (ARINC) Communications and Retrieval System (ACARS) (Cornman and Mahoney,

1991) and surface temperature measurements from the Automated Surface Observation System (ASOS). Real-time soundings constructed in this way will be used in the FAA Integrated Terminal Weather System Microburst prediction algorithm (Wolfson, personal communication).

More investigations of the effect of the stable layers on outflow strength should be done to determine a value of decrease in outflow strength based on the strength of the stable layer in various environments. If ACARS or some other measurement capability is determined to give accurate information that can assist in evaluating the strength of a stable layer, then the incorporation of this information into TDWR and NEXRAD algorithms could possibly increase the accuracy of predictions in some environments.

BIBLIOGRAPHY

Biron, P.J. and M.A. Isaminger, 1991: High resolution microburst outflow vertical profile data from Huntsville, AL and Denver, CO. Lincoln Laboratory Project Report ATC-163, 214 pp.

Braham, R.R., 1952: The water and energy budgets of the thunderstorm and their relation to thunderstorm development. *J. Meteor.*, 9, 227-242.

Browning, K.A., 1964: Airflow and precipitation trajectories within severe local storms which travel to the right of the winds. *J. Atmos. Sci.*, **21**, 634-639.

Campbell, S.D., 1991: Performance results and potential operational uses for the prototype TDWR microburst prediction product. Preprints, *4th International Conference on Aviation Weather Systems*, Paris, Amer. Meteor. Soc., J33-J36.

Campbell, S.D. and M.A. Isaminger, 1990: A prototype microburst prediction product for the Terminal Doppler Weather Radar. Preprints, *16th Conference Severe Local Storms*, Kananaskis Park, Amer. Meteor. Soc., 393-396.

Chen, J.P., 1986: A numerical simulation of microbursts. M.S. thesis, South Dakota School of Mines and Technology, 118 pp.

Cornmam, L. and W. Mahoney, 1991: Integration of the TDWR and LLWAS wind shear detection systems. *4th International Conference on Aviation Weather Systems*, Paris, Amer. Meteor. Society, J27-J32.

Droegemeier, K.D., 1992: A "numerical field experiment" approach to the prediction of downdraft-induced low-level wind speeds with application to microbursts. Part I: Solution characteristics. Accepted to *Mon. Wea. Rev.*

Droegemeier, K.K., ·1991: Development of an expert system for the Honeywell Windshear Computer using data from a numerical thunderstorm model. Final report, 1991, 63 pp.

Eilts, M.D., 1987: Nowcasting low-altitude wind shear with a Doppler radar. Preprints, *25th AIAA Aerospace Sciences Meeting*, Reno, 5 pp.

Eilts, M.D. and S.K. Oakland, 1989: Convergence aloft as a precursor to microbursts. Preprints, *24th Conference on Radar Meteorology*, Tallahassee, Amer. Meteor. Soc., 190-193.

Eilts, M.D., S.H. Olson, G.J. Stumpf, L.G. Hermes, A. Abrevaya, J.Culbert, K.W. Thomas, K. Hondl, and D. Klingle-Wilson, 1991: An improved gustfront detection algorithm for the TDWR. Preprints, *4th International Conference on Aviation Wea. Systems*, Paris, Amer. Meteor. Soc., J37-J42.

Fujita, T.T. and H.R. Byers, 1977: Spearhead echo and downburst in the crash of an airliner. *Mon. Wea. Rev.*, **105**, 129-146.

Greene, D.R. and R.A. Clark, 1972: Vertically integrated liquid water: A new analysis tool. *Mon. Wea. Rev.*, **100**, 548-552.

Hjelmfelt, M.R., 1988: Structure and life cycle of microburst outflows observed in Colorado. *J. Appl. Meteor.*, **27**, 900-927.

Isaminger, M.A., 1988: A preliminary study of precursors to Huntsville microbursts. Lincoln Laboratory Project Report ATC-153, 21 pp.

Johnson, J.T., 1992: Investigation of outflow strength variability in Florida downburst-producing storms. M.S. Thesis, School of Meteorology, University of Oklahoma, 172 pp.

Klemp, J.B. and R.B. Wilhelmson, 1978: The simulation of three-dimensional convective storm dynamics. *J. Atmos. Sci.*, **35**, 1070-1096.

Knupp, K.R., 1985: Precipitating convective cloud downdraft structure: A synthesis of observations and modeling. Ph.D. dissertation, Colorado State University, 296 pp.

Krueger, S.K., and R.M. Wakimoto, 1985: Numerical simulations of dry microbursts. Preprints, *14th Conference on Severe Local Storms*, Indianapolis, Amer. Meteor. Soc., 163-166.

Krueger, S.K., R.M. Wakimoto, and S.J. Lord, 1986: Role of ice-phase microphysics in dry microburst simulations. Preprints, *23rd Conference on Radar Meteorology*, Snowmass, Amer. Meteor. Soc., J73-J76.

Krumm, W.R., 1954: On the cause of downdrafts from dry thunderstorms over the plateau area of the United States. *Bull. Amer. Meteor. Soc.*, **35**, 122-125

Merritt, M.W., 1987: Automated detection of microburst wind shear for the Terminal Doppler Weather Radar. S.P.I.E, 846.

Proctor, F.H., 1988: Numerical simulations of an isolated microburst. Part I: Dynamics and structure. *J. Atmos. Sci.*, **45**, 3137-3160.

Proctor, F.H., 1989: Numerical simulations of an isolated microburst. Part II: Sensitivity experiments. *J. Atmos. Sci.*, **46**, 2143-2165.

Roberts, R.D. and J.W. Wilson, 1986: Nowcasting microburst events using single Doppler radar data. Preprints, *23rd Conference on Radar Meteorology*, Snowmass, Colorado, Amer. Meteor. Soc., 14-17.

Shantz, A. 1991: The Federal Aviation Administration (FAA) and the National Weather Service (NWS) modernization programs: Catalysts for change in weather services. Preprints, *4th International Conference on Aviation Weather Systems*, Paris, 56-59.

Srivastava, R.C., 1985: A simple model of evaporatively driven downdraft: Application to a microburst downdraft. *J. Atmos. Sci.*, **42**, 1004-1023.

Stewart, S.R., 1991: The prediction of pulse-type thunderstorm gusts using vertically integrated liquid water content (VIL) and the cloud top penetrative downdraft mechanism. NOAA Tech. Memo. NWR SR-136. National Weather Service, 20 pp.

Stoll, S.A. 1991: Microburst detection by the Low-Level Wind Shear Alert System. *Weather*, **46**, 334-347.

Straka, J.M., 1992: A cloud/mesoscale model for detailed studies of precipitation development. Part I: Formulations and benchmark simulations. To be submitted to *J. Atmos. Sci.*.

Straka, J.M., 1989: Hail growth in a highly glaciated central high plains multi-cellular hailstorm. Ph.D. dissertation, University of Wisconsin-Madison, 413 pp.

Straka, J.M. and J.R. Anderson, 1992: Numerical simulations of microburst producing storms: Some results from storms observed during COHMEX. Submitted to *J. Atmos. Sci.*.

Tripoli, G.J., and W.R. Cotton, 1986: An intense, quasi-steady thunderstorm over mountainous terrain. Part IV: Three-dimensional numerical simulation. *J. Atmos. Sci.*, **43**, 894-912.

Wilson, J.W., R.D. Roberts, C. Kessinger, J. McCarthy, 1984: Microburst wind structure and evaluation of Doppler radar for airport wind shear detection. *J. Climate and Appl. Meteor.*, **23**, 898-915.

Wolfson, M., 1990: Understanding and predicting microbursts. Ph.D dissertation. Massachusetts Institute of Technology. 303 pp.